Smart placement of depolluting panels in urban areas as regards of the airflow using adjoint framework and district digital twin

T. Hamada, F. Chabi, R. Chakir, D. Lejri, F. Dugay, J. Waeytens

Smart placement of depolluting panels in urban areas as regards of the airflow using adjoint framework and district digital twin

T. Hamada[a], F. Chabi[a], R. Chakir[a], D. Lejri[b], F. Dugay[c], J. Waeytens[a,*]

[a] *Univ Gustave Eiffel, COSYS, , F-77420, Champs-sur-Marne, France*
[b] *Univ Lyon, Univ Gustave Eiffel, ENTPE, LICIT-Eco7, , F-69675, Lyon, France*
[c] *Airparif, F-75004, Paris, France*

Abstract

A two-step numerical strategy based on a district digital twin is presented to efficiently deploy a limited number of depolluting panels in urban areas. In a diagnosis stage, a detailed pollutant concentration map is computed using CFD to identify critical highly polluted areas. Then, in a remediation stage, the optimal placement of depolluting panels as regards of urban airflow is determined to locally mitigate the air pollution in the exposed areas. For this purpose, a spatial sensitivity indicator calculated from an adjoint framework is proposed. The approach is applied to two real case studies: the full-scale laboratory district "Sense-City" under controlled conditions and a district area in Paris using realistic NOx traffic emission and wind conditions. In both case studies, it is shown that depolluting panels should be placed on a part of the sidewalks, the building facades and the roads adjacent to the sidewalks to reduce the high NOx concentration on some sidewalks and on first-floor building windows, thus preventing outdoor/indoor pollutant transfer. It is also proven that the proposed strategy is more efficient than a non-smart massive deployment of depolluting panels to improve the air quality in exposed areas. In addition to practical recommendations, this numerical strategy can provide a help-decision tool for city managers to design depolluting panels-based mitigation actions.

Keywords: outdoor air quality, traffic pollution, depolluting panels, CFD, adjoint problem, digital twin, real-case study

*corresponding author email: julien.waeytens@univ-eiffel.fr

1. Introduction

Air pollution is a major public health problem. According to the World Health Organization, about 4.2 million deaths per year are related to poor air quality (World Health Organization, 2016). A wide variety of sectors, *e.g.* traffic, industry, agriculture, and housing, contribute to air pollution. Urban cities produce around 78% of CO_2 and atmospheric pollutants that affect 50% of the population living in these areas (Bereitschaft and Debbage, 2013). The main pollutants in outdoor air are NOx (NO_2+NO), VOC, SO_2, CO, O_3, and PM. Traffic is an important contributor to NOx emission in cities (U.S. Environmental Protection Agency, 1999; Mishra and Goyal, 2015). It has been shown that short or long-term human exposure to nitrogen dioxide (NO_2) causes respiratory and cardiovascular diseases (Stafoggia et al., 2022; Meng et al., 2021). Through apartment openings, it can be noted that outdoor pollutants can also affect indoor air quality (Leung, 2015). It is therefore important to (i) understand how these pollutants are dispersed in the urban environment by making detailed cartographies, (ii) identify the critical areas where pollution is high, and (iii) propose an appropriate strategy to improve the air quality. These three items are the main issues to be addressed in the article.

Due to the significant financial cost, only a limited number of air quality stations are deployed in cities and regions to get accurate measurements. Physical models and numerical simulations can be employed to counterbalance the sparse coverage of the instrumentation. Hence, data assimilation techniques combining sensor outputs and physical models are often considered to get accurate air pollutant cartography (Tilloy et al., 2013; Elbern and Schmidt, 2001; Le Dimet and Talagrand, 1986). In region *Ile de France*, the Airparif agency combines the chemistry-transport model CHIMERE (Bessagnet et al., 2008) at the regional scale and the Gaussian dispersion model ADMS-Urban (Carruthers et al., 1994) at the district scale to produce maps at a resolution ranging from 12.5m to 50m. The different sources of pollutants, and in particular traffic-related emissions, are calculated with the model HEAVEN. These models enable numerical predictions at a reasonable computational cost; however they are not appropriate for air pollutant cartography at smaller resolution. When designing efficient urban planning,

using virtual testing strategies to locally reduce highly polluted areas, more sophisticated models such as "Computational Fluid Dynamics" can be considered. They can provide air pollutant cartography at the meter resolution. CFD has been used to get a better understanding of the urban airflow and the pollutant dispersion around building in urban areas (Ramponi et al., 2015; Tominaga and Stathopoulos, 2013; Di Sabatino et al., 2013; Gousseau et al., 2011; Hang et al., 2011), practical recommendations can be found in (Tominaga and Stathopoulos, 2016). Special attention has been given to street canyons (Koutsourakis et al., 2012; Tominaga and Stathopoulos, 2011; Di Sabatino et al., 2008) where turbulences induced by traffic (Zheng and Yang, 2021; Zhao et al., 2021; Solazzo et al., 2008) , the roof shapes (Yassin, 2011) and the vegetation (Salim et al., 2011; Balczo et al., 2009; Gromke et al., 2008) were studied. An overview of CFD studies in street canyon applications is proposed in the review article (Li et al., 2006). To predict turbulent flows in an urban environment, steady or unsteady Reynolds Averaged Navier-Stokes (RANS or URANS, see (Rodriguez, 2019)) and Large Eddy Simulation (LES, see (Sagaut, 2006)) are commonly employed. Despite their lack of accuracy compared to LES model (Gousseau et al., 2011), RANS models remain largely used in operational studies due to their lower computational cost (Blocken, 2015). In the present article, RANS models are to be considered to get a detailed NO_x pollution map at the street and the district scales.

After identifying the critical highly polluted areas from detailed CFD air quality maps, actions have to be carried out to reduce human exposure to pollutants in these areas. Herein, the focus is on traffic pollution. The different types of mitigation strategies can be divided into three categories, based on the partial differential equation (1) representing transport-diffusion-reaction

$$\frac{\partial C}{\partial t} + \underbrace{\vec{\mathrm{v}} \cdot \nabla C - div(D \nabla C)}_{II} + \underbrace{R(C)}_{III} = \underbrace{S}_{I} \tag{1}$$

where C is the pollutant concentration, $\vec{\mathrm{v}}$ and D are the flow velocity and the diffusion parameter, $R(C)$ represents chemical reaction of species and S is associated to source emissions.
As shown in Eq (1), obviously the pollutant concentration C can be decreased by reducing the source emission S. This strategy "I" is often employed by municipalities and regional authorities via traffic restrictions like Low-Emission

Zone (LEZ) and the replacement of a portion of the oldest vehicles. A good knowledge of the local fleet and the virtual testing of different scenarios *via* a simulation platform are recommended to efficiently design the Low-Emission Zones (Andre et al., 2020; André et al., 2018; Duque et al., 2016).
The strategy "II" deals with the improvement of urban ventilation. For that, a first way is to change the urban morphology. In the literature, numerous researches have shown the effects of the urban morphology at the building, the street and the district scales on the air quality (da Silva et al., 2022; Yang et al., 2020; An et al., 2019; Shen et al., 2017). At the district scale, the mitigation of air pollution through urban morphology adjustments can be performed in new districts or in local urban renewal, *e.g.* demolition of old buildings to create wind corridors to improve air quality and thermal comfort (Peng et al., 2015). These actions can be long-term and expensive. At the street scale, the installation of continuous, impermeable, high (more than 2 meters height) barriers near traffic roads, *e.g.* solid walls or green barriers with very low porosity/permeability can reduce the air pollution on the sidewalk especially in street canyon (Issakhov and Omarova, 2021; Gromke et al., 2016; Vos et al., 2013; Hagler et al., 2011). Vegetation is also used as nature-based solutions for various purposes, *e.g.* heat island phenomena, noise reduction, preservation of biodiversity and the contribution of human well-being. Trees in streets and more generally urban parks have a positive global impact on city air pollution, but they can be locally counterproductive (Xing and Brimblecombe, 2019; Selmi et al., 2016). On the one hand, the pollutant concentrations can be reduced *via* the absorption and the deposition on leaves. On the other hand, the presence of trees can modify the pollutant dispersion by obstructing the urban airflow. Still at the street scale, the urban airflow can also be modified using passive or active ventilation strategies. In (Mirzaei and Haghighat, 2010), a pedestrian ventilation system is proposed to enhance the air quality and thermal comfort in the pedestrian walking area of street canyons. It guides polluted air from the near-surface level through a designed vertical duct system to the surrounding street level.
Lastly, the air quality improvement strategy "III" is based on the degradation of pollutant species via a chemical reaction mechanism. In the last decade, the depollution structures made of the integration of photocatalyst semiconductor oxides such as titanium dioxide (TiO_2) and zinc oxide (ZnO) in construction materials or as direct use on a surface layer, have been used to remove various pollutants (O3, COx, NOx, VOCs) (Le Pivert et al., 2021; Darvish et al., 2020; Le Pivert et al., 2020; Binas et al., 2017). The func-

tioning of these panels relies on the photocatalysis mechanism. Thus, with sufficient light and under the presence of photocatalyst (ZnO or TiO_2), a catalytic oxidation effect is triggered, degrading certain polluting particles (He et al., 2017; Garrido et al., 2019). Also, despite that TiO_2 photocatalyst in the form of nanoparticles is the most used for the production of depolluting surfaces, recent studies are moving towards the use of other photocatalysts such as ZnO given the harmful effect of TiO_2 on health and the environment (Grande and Tucci, 2016; Wu and Ren, 2020). For these reasons (Le Pivert et al., 2021) developed depolluting panels, which consist of photocatalyst nanostructures ZnO grown on construction materials (tiling, rock aggregates), and showed that the air pollution from road traffic is locally reduced when placing them on the road surfaces.

Given the very encouraging results of the depolluting panels in locally reducing urban pollution, it can be promising to deploy them in urban areas. They can be placed as removable paving blocks on road surfaces, building walls, motorway sound barriers, etc. To concretely evaluate the potential of pollutant elimination by photocatalytic coatings in a street canyon, the authors in (Pulvirenti et al., 2020) conducted CFD simulations and experimental validation in Bologna, Italy. To go one step further in this article, a complete chain approach from the detailed cartography of air pollutants to the smart placement of depolluting panels is proposed. The main contribution herein concerns the optimal placement of a restricted surface of depolluting panels through a CFD-based strategy in order to locally improve the air quality in critical urban areas. The article is organized as follows. The two-step computer-aided strategy for the smart placement of depolluting panels is presented in Section 2. First CFD is used, in a *diagnosis* step, to identify critical highly polluted areas at the district scale. Then, in a *remediation* step, a virtual testing strategy based on CFD and an adjoint framework is developed to determine a relevant placement of depolluting panels for goal-oriented air pollutant mitigation. In Section 3, the results of our numerical strategy on a controlled laboratory district, named "Sense-City", are analysed. In Section 4, the smart placement strategy is applied to a Paris district under *in-situ* meteorological and traffic conditions.

2. Numerical method for the optimal placement of depolluting system as regards of urban airflow

2.1. Outline

In this section an overview of our two-step virtual testing strategy to determine a smart placement of depolluting panels at the district scale is given. Our approach relies on the formulation of an optimization problem and a sensitivity analysis through the adjoint framework. The main steps of the proposed method are summarized below.

Diagnosis stage:
The goal is to identify the highly polluted areas in the studied district from detailed pollution cartographies.

- Computation of the airflow at the district scale using computational fluid dynamics;
- Solving the direct advection-diffusion reaction model to reconstruct precisely the pollution map at the district scale;
- Identification of the critical areas where people can be exposed to high level of pollutants from the pollution map. The pollutant concentrations in these critical areas are defined as quantities of interest.

Remediation stage:
The objective is to improve air quality in the determined critical areas by decreasing the quantity of interest. Local sensitivity analysis is performed for the selected quantity of interest considering both direct and adjoint problems in the original urban configuration (without depolluting panels).

- Solving the adjoint advection-diffusion reaction problem associated with the chosen quantities of interest;
- Computation of the spatial sensitivity indicator using the concentration determined in the diagnosis stage and the numerical solution of the adjoint problem;
- Selection of a relevant position of depolluting panels given by significant value of the sensitivity indicator.

Each of these steps is detailed in the following sections.

2.2. Technical description

2.2.1. Diagnosis: district pollutant map using direct model

The computational domain of the district is denoted Ω. After simulating the airflow $\vec{\mathrm{v}}$ over Ω, the detailed cartography of the pollutant concentration $C(\mathbf{x}, t)$ is obtained by solving the convection-diffusion-reaction equation:

$$\begin{cases} \dfrac{\partial C}{\partial t} + \vec{\mathrm{v}} \cdot \nabla C - div(D \nabla C) + R(C) = S \quad \text{in} \quad \Omega \times [0, T] \\ C = C_i \quad \text{on} \quad \Gamma_i \times [0, T] \\ \nabla C \cdot \vec{n} = 0 \quad \text{on } \Gamma_o \cup \Gamma_w \times [0, T] \\ C(t = 0) = C_0 \quad \text{in} \quad \Omega \end{cases} \tag{2}$$

where C_i and C_0 denotes respectively the background concentration entering the domain Ω through the inlets Γ_i and the initial concentration in the domain. The boundaries Γ_o and Γ_w are associated with outlet and wall surfaces.

In urban air quality applications, the airflow is considered Newtonian, incompressible and turbulent. In practice, the airflow velocity $\vec{\mathrm{v}}$ and the turbulent viscosity μ_t $(kg/(m.s))$ are obtained from Reynolds Averaged Navier-Stokes simulations (RANS). The diffusion term D appearing in Eq. (2) is the sum of the molecular diffusion and the turbulent diffusion D_t. The turbulent diffusion D_t (m^2/s) is given by the formula

$$D_t = \frac{\mu_t}{\rho \; Sc_t}, \tag{3}$$

where ρ (kg/m^3) is the density of air and Sc_t is the turbulent Schmidt number. Lastly, $R(C)$ and S in Eq.(2) are the reaction and the source terms. The source term S in the domain Ω is used to define the position and the amplitude of source emissions.

In the applications to be presented in Sections 3 and 4, the pollutant cartography is obtained from the deterministic solution of the direct problem. To better take into account the uncertain parameters of the physical model like boundary air flow conditions and source term characteristics, uncertainty quantification (UQ) and data assimilation can be considered (see,(Hammond et al., 2019; Mons et al., 2017; Tilloy et al., 2013)).

The critical areas where people are exposed to high pollution levels are determined from the detailed pollutant concentration map $C(x,t)$. Hence, the concentrations in these critical areas are defined as quantities of interest $\mathcal{J}$.

$$\mathcal{J} = \int_0^T \int_\Omega f_q(\mathbf{x})\, \xi(t)\, C(\mathbf{x},t)\, \mathrm{d}\Omega\, \mathrm{d}t, \tag{4}$$

where $f_q(\mathbf{x})$ is the space function to extract the pollution in a critical area Ω_q and $\xi(t)$ is the time extractor function to define the period of interest. In our case, the pollutant concentration at the location where we want to improve the air quality is chosen as a quantity of interest. Thereby, herein Ω_q is a subdomain of Ω representing the location where improved air quality is desired.

2.3. Remediation: Smart placement of depolluting panels solving minimization problem

To model the effects of depolluting panels on the district air quality, the advection-diffusion reaction equations is considered:

$$\begin{cases} \dfrac{\partial C}{\partial t} + \vec{\mathbf{v}} \cdot \nabla C - div(D \nabla C) = S \quad \text{in} \quad \Omega \times [0,T] \\ C = C_i \quad \text{on} \quad \Gamma_i \times [0,T] \\ \nabla C \cdot \vec{\mathbf{n}} = 0 \quad \text{on} \quad \Gamma_o \cup \Gamma_n \times [0,T] \\ -D \nabla C \cdot \vec{\mathbf{n}} = kC \quad \text{on} \quad \Gamma_p \times [0,T] \\ C\,(t=0) = C_0 \quad \text{in} \quad \Omega \end{cases} \tag{5}$$

To remain simple, the degradation of the pollutant by the photocatalytic depolluting system is described using a first-order reaction,

$$-D \nabla C \cdot \vec{\mathbf{n}} = kC \quad \text{on} \quad \Gamma_p \times [0,T],$$

where k (m/s) denotes the reaction rate function. The reaction rate is an approximation of Langmuir-Hinshelwood kinetic model and was used in previous works (Pulvirenti et al., 2020; Yusuf et al., 2020; Yusuf and Palmisano, 2021). The degradation reaction occurring at the surfaces of the depolluting panels, it is considered as a boundary condition (Yusuf et al., 2020; Yusuf and Palmisano, 2021). For operational reasons, the depolluting panels can not be placed on any surfaces of the district. Consequently, the potential placement of depolluting panels is limited to the boundary Γ_p which is a restricted part

of the wall boundary Γ_w. The boundaries Γ_p and Γ_n are defined such that $\Gamma_w = \Gamma_p \cup \Gamma_n$. Lastly, let us underline that $k(\mathbf{x})$ is a scalar field defined on the boundary Γ_p.

The constrained minimization problem to be solved is:

$$\min_{k, C \in \mathcal{C}} \mathcal{J}(C, k) \tag{6}$$

where the constraint "$C \in \mathcal{C}$" imply that the concentration C has to satisfies the direct problem (5). The Lagrangian function $\mathcal{L}$ associated to the constrained minimization problem (6) can be written as

$$\begin{aligned}\mathcal{L}(C, k; \lambda) = \mathcal{J}(C, k) - \int_0^T \int_\Omega \lambda_1 \left(\frac{\partial C}{\partial t} + \vec{\mathbf{v}}.\nabla C - div(D\nabla C) - S \right) \mathrm{d}\Omega \, \mathrm{d}t \\ - \int_0^T \int_{\Gamma_i} \lambda_2 (C - C_i) \mathrm{dS} \, \mathrm{d}t - \int_0^T \int_{\Gamma_o \cup \Gamma_n} \lambda_3 \nabla C \cdot \vec{\mathbf{n}} \, \mathrm{dS} \, \mathrm{d}t \\ + \int_0^T \int_{\Gamma_p} \lambda_4 (D\nabla C \cdot \vec{\mathbf{n}} + kC) \mathrm{dS} \, \mathrm{d}t - \int_\Omega \lambda_5 (C(t=0) - C_0) \mathrm{d}\Omega\end{aligned} \tag{7}$$

where λ_i, $i \in \{1, .., 5\}$ are the Lagrange multipliers.

Finding the minimum of the functional $\mathcal{J}$ with the constraint $C \in \mathcal{C}$ is equivalent to finding the stationary points of the Lagrangian functional $\mathcal{L}$ (7) as a function of the Lagrange multipliers λ_i, C and k meaning

$$\frac{\partial \mathcal{L}}{\partial \lambda_i} = \frac{\partial \mathcal{L}}{\partial C} = \frac{\partial \mathcal{L}}{\partial k} = 0$$

The partial derivation of the Lagrangian $\mathcal{L}$ according to the Lagrange multipliers λ_i, *i.e.* $\partial \mathcal{L} / \partial \lambda_i = 0$, gives as expected the "direct problem" (5) satisfied by the concentration C. As for the partial derivation of $\mathcal{L}$ according to the concentration C, *i.e.* $\partial \mathcal{L} / \partial C = 0$, leads to the formulation of the "adjoint problem", with the adjoint concentration state noted $\tilde{C}$ that satisfies

$$\begin{cases} -\dfrac{\partial \tilde{C}}{\partial t} - \vec{\mathbf{v}} \cdot \nabla \tilde{C} - div(D \nabla \tilde{C}) = f_q \, \xi \quad \text{in} \quad \Omega \times [0,T] \\ \tilde{C} = 0 \quad \text{on} \quad \Gamma_i \times [0,T] \\ \nabla \tilde{C} \cdot \vec{\mathbf{n}} = 0 \quad \text{on} \quad \Gamma_n \times [0,T] \\ -D \nabla \tilde{C} \cdot \vec{\mathbf{n}} = k \tilde{C} \quad \text{on} \quad \Gamma_p \times [0,T] \\ D \nabla \tilde{C} \cdot \vec{\mathbf{n}} + (\vec{\mathbf{v}} \cdot \vec{\mathbf{n}}) \, \tilde{C} = 0 \quad \text{on} \quad \Gamma_o \times [0,T] \\ \tilde{C}(t = T) = 0 \quad \text{in} \quad \Omega. \end{cases} \tag{8}$$

The main steps of the calculations to obtain the adjoint problem are given in Appendix A.

The adjoint problem corresponds to a backward advection-diffusion equation which involves a fictitious source emission located in the area of interest Ω_q. Even in stationary conditions, the adjoint problem is different from the direct problem (5). The adjoint concentration state $\tilde{C}$ corresponds to a sensitivity function associated with the considered quantity of interest $\mathcal{J}$. Hence, if the adjoint state is null in a part of the domain, it physically means that what happens in this part of the domain will not affect the chosen quantity of interest. This type of adjoint model was previously used by the authors to study the optimal placement of air quality sensors (Waeytens and Sadr, 2018).

Lastly, the partial derivation of $\mathcal{L}$ according to the reaction rate scalar field k gives the sensitivity of the quantity of interest $\mathcal{J}$ to the depolluting panels and satisfies

$$\frac{\partial J}{\partial k} = \frac{\partial \mathcal{L}}{\partial k} = \int_0^T \lambda_4 \, C \mathrm{dt} = - \int_0^T \tilde{C} C \mathrm{dt} \quad \text{on} \quad \Gamma_p \tag{9}$$

As shown in Appendix A, one has $\lambda_4 = -\tilde{C}$ on $\Gamma_p \times [0,T]$.

To evaluate the effectiveness of depolluting panels placed at a position $\mathbf{x}$, a positive sensitivity indicator is defined:

$$I(\mathbf{x}) = \left| \frac{\partial J}{\partial k} \right| = \int_0^T \tilde{C}(\mathbf{x},t) C(\mathbf{x},t) dt \tag{10}$$

Let us note that the indicator $I(x)$ is significant when both direct concentration C and the adjoint concentration $\tilde{C}$ have high values. The depolluting panels must therefore be placed in high-polluted zones ($C(x,t)$ high) which can impact the chosen quantity of interest ($\tilde{C}$ high) due to the transport and

the dispersion of the pollutant.

In the following sections, the spatial sensitivity indicator $I(\mathbf{x})$ will be used to select an efficient placement of depolluting panels for two urban applications. For an operational purpose and an objective of limiting computational cost, we only perform a local sensitivity analysis by solving the direct problem (5) and the adjoint problem (8) in the pre-existing configuration, *i.e.* no depolluting panels ($k = 0$). Then, the direct and adjoint numerical solutions are used to evaluate the sensitivity indicator (10) on all the surfaces of Γ_p. Finally, the depolluting panels are to be placed only on surfaces where the indicator $I(\mathbf{x})$ is significant.

3. Application in controlled conditions: the Sense-City district

To illustrate our approach, a controlled scenario in a full-scale small district embedded in the climatic chamber of the equipment "Sense-City" is first considered. In this part, the airflow within the climatic chamber is considered steady and turbulent (Streichenberger et al., 2021). The numerical study addresses the transient dispersion of a non-reactive gas pollutant emitted at a given position on the road of the Sense-City district within a period of 180 seconds[1]. In what follows, the detailed description of the controlled scenario in Sense-City district and the application of depolluting panels strategic position are presented.

3.1. Presentation of Sense-City equipment and the studied district under controlled conditions

Sense-City is an instrumented district built in 2018 and located on the campus of Université Gustave Eiffel at Champs-sur-Marne, France (Derkx et al., 2012). This district is designed for the validation of numerical physical models and innovative technologies used in the field of urban environments. It is composed of two small districts of $400\,\mathrm{m}^2$. These urban areas can be studied in natural conditions or in controlled climatic conditions using a large mobile climatic chamber of dimension ($20\,\mathrm{m} \times 20\,\mathrm{m} \times 10\,\mathrm{m}$). In addition, more than 150 sensors (temperature sensors, gas sensors, etc..) are

[1]Due to the closed-cycle air circulation within the climatic chamber (Streichenberger et al., 2021), the simulation period is limited to 180 seconds.

installed at different locations in the district.

In the present article, the small district #1 covered by the climatic chamber is used for our numerical study (see Figure 1). It consists of two small houses, a two-story precast concrete building and roads. Figure 1 also shows the digital twin of this district. On the south and north walls of the climatic chamber are installed six fans, two horizontal air-forced ducts and two vertical rectangular columns for air extraction called "extractor". The boundary surfaces of the computational domain are: inlet fans (surfaces with red and blue colors), outlet fans (surfaces with green color), horizontal air-forced ducts (surfaces with black and purple colors), extractors (surfaces with yellow) and walls (buildings and climatic chamber walls). For more details about the airflow characteristics, turbulent air flow simulation using RANS model and its validation using 3D anemometer measurement, the reader can refer to (Streichenberger et al., 2021).

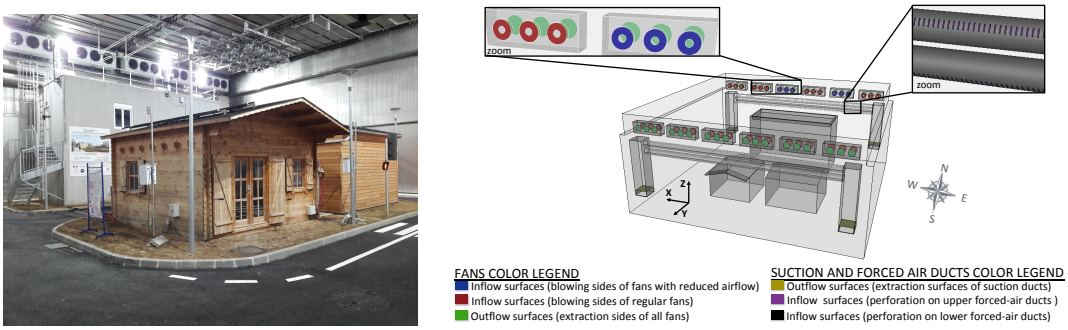

Figure 1: Sense-City district #1 covered by the climatic chamber (at left) and its associated digital twin (at right).

.

3.2. Time evolution cartography of the pollutant dispersion in a controlled scenario without depolluting system

In this first application, the time-evolution of the concentration in Sense-City district in controlled conditions on the time interval $[0, 180s]$ is studied. Concerning the Sense-City numerical mock-up, let us note that the center of the Cartesian coordinate system, represented in Fig. 2, is placed on the ground surface at the center of the district such that the district domain is

described by $\{x \in [-11.22\text{m}, 11.22\text{m}],\ y \in [-11.1\text{m}, 11.1\text{m}],\ z \in [0\text{m}, 10\text{m}]\}$. Herein, the scenario of a continuous release of a pollutant tracer, *i.e.* non-reactive, from a parallelepiped volumic source ($0.5 \times 0.5 \times 0.5 = 0.125\,\text{m}^3$) is considered. The center of the source is located in the middle of the road at the coordinates ($x = 0\,\text{m}, y = -2.5\,\text{m}, z = 1\,\text{m}$) between the concrete building and the two houses (see Fig. 2) at height $z = 1\,\text{m}$. The parallelepiped volume Ω_s of the source is expressed by the space function f_s:

$$f_s(\mathbf{x}) = \begin{cases} 1 & \text{for } \mathbf{x} \in \Omega_s \\ 0 & \text{elsewhere} \end{cases} . \tag{11}$$

The source amplitude is taken to 2000 $\mu\text{g/m}^3\text{/s}$. The volume of the source being of 0.125 m^3, the considered emission is 250 $\mu\text{g/s}$ which corresponds to the order of magnitude of NOx mean emission at 20km/h for EURO 6 passengers cars with a small petrol engine, *i.e.* 0.039g/km emission factor that gives a value of 217 $\mu\text{g/s}$ (Ntziachristos et al., 2009).

In the absence of depolluting system, to determine the time-evolution cartography of the pollutant, the direct advection-diffusion problem defined in Eq. (2) is solved. Since the pollutant concentration $C(\mathbf{x}, t)$ is considered herein as a passive scalar, *i.e.* non-reactive pollutant such as in the articles (Tee et al., 2020; Tominaga and Stathopoulos, 2018), the reaction term in Eq. (2) is taken to 0.
The time-averaged turbulent velocity field $\vec{\mathbf{v}}$ and the turbulent viscosity μ_t are obtained from a previous work (Streichenberger et al., 2021), where unsteady Reynolds Averaged Navier-Stokes (URANS) turbulent model within software Code_Saturne was used to simulate airflow in Sense-City district. The turbulent diffusion is $D_t = \mu_t/(\rho S_c)$ and the Schmidt number S_c is set to 0.7 (Tominaga and Stathopoulos, 2007; Wang and McNamara, 2006). Null initial concentration, homogeneous Dirichlet conditions (*i.e.* $C_0 = C_i = 0$) at the inlets (inlet fans, horizontal air-forced ducts) and homogeneous Neumann condition (*i.e.* $\nabla C \cdot \vec{\mathbf{n}} = 0$) on the walls and outlets are considered.

In this application, the Finite Element Method with SUPG stabilization in the software FreeFem++ (Hecht, 2012) is used to solve the direct gas

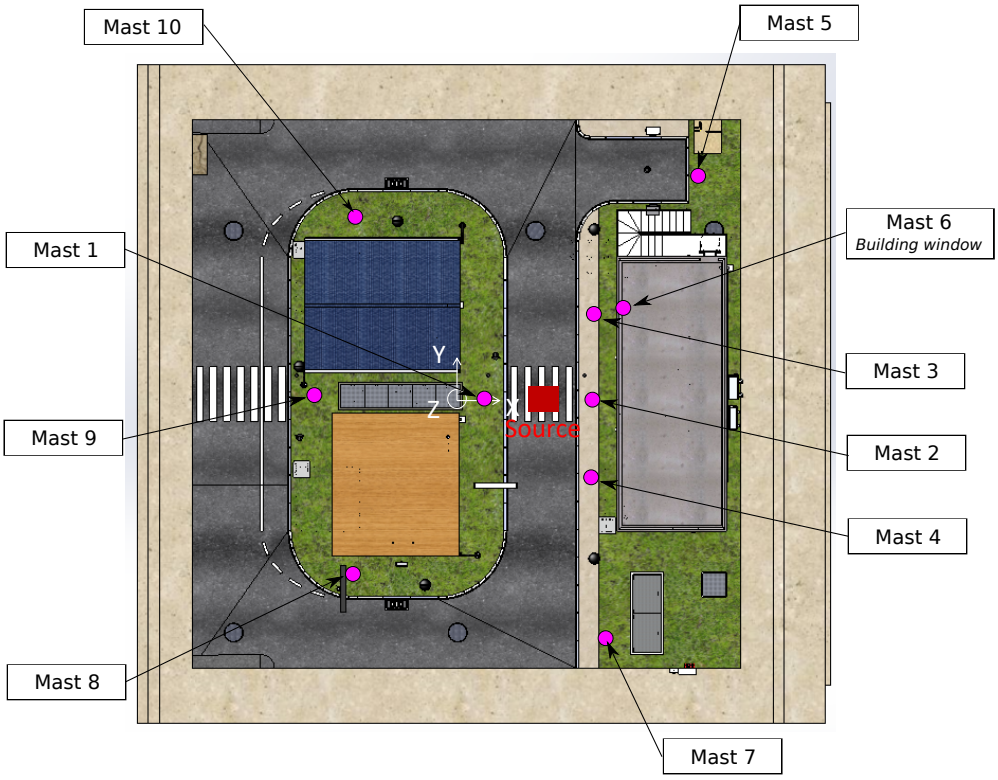

Figure 2: Position of the pollutant source and the mast sensors in Sense-City district.

.

dispersion model Eq. (2). The variational formulation of the problem reads:

$$\begin{aligned}\int_\Omega \frac{\partial C}{\partial t} C^* \,\mathrm{d}\Omega \;&+\; \int_\Omega (\vec{\mathbf{v}}\cdot\nabla C)C^* \,\mathrm{d}\Omega + \int_\Omega \mathcal{D}(\nabla C\cdot\nabla C^*)\,\mathrm{d}\Omega \\ &- \int_{\partial\Omega} \mathcal{D}(\nabla C\cdot\vec{\mathbf{n}})C^*\,\mathrm{d}\Omega + \alpha\int_\Omega \frac{\partial C}{\partial t}(\vec{\mathbf{v}}\cdot\nabla C^*)\,\mathrm{d}\Omega \\ &+ \alpha\int_\Omega (\vec{\mathbf{v}}\cdot\nabla C)(\vec{\mathbf{v}}\cdot\nabla C^*)\,\mathrm{d}\Omega \quad - \alpha\int_\Omega \mathcal{D}\Delta C(\vec{\mathbf{v}}\cdot\nabla C^*)\,\mathrm{d}\Omega \\ &= \int_\Omega f C^*\,\mathrm{d}\Omega \quad + \alpha\int_\Omega f(\vec{\mathbf{v}}\cdot\nabla C^*)\,\mathrm{d}\Omega \end{aligned} \tag{12}$$

where α represents the stabilization term defined by SUPG method (Hughes et al., 1986; Franca et al., 1992). Euler implicit scheme is used for the time

discretization. The time step is taken to $\Delta t = 0.1\,\mathrm{s}$.
An unstructured mesh with a local volume refinement around the source emission was built using the open-source software SALOME with the automatic mesh generator NETGEN. The mesh has a total cell number of about 3,947,186.

In Fig. 3, the spatial maps of pollution in the Sense-City district are plotted at pedestrian level ($\mathrm{z} = 1.5\,m$) for different times ($\mathrm{t} = 5\,s$; $\mathrm{t} = 30\,s$; $\mathrm{t} = 60\,s$). The vertical profile of pollutant concentration along the south-oriented building wall which faces the road is also represented. Since the concentration remains almost unchanged after 60 seconds, only the pollutant maps from $\mathrm{t} = 0\,s$ to $\mathrm{t} = 60\,s$ are given. In Fig. 4, the numerical concentration at monitoring points (see Fig. 2) are provided as well to illustrate the time evolution of the concentration distribution. As the concentration was negligible at Masts 7, 8, 9 and 10, they are not represented in Fig. 4.
From Fig. 3, it can be noted that the pollutant goes from the source to the concrete building and then bypasses it on one side and goes towards the extractor of Sense-City ventilation system, which is located in the lower right corner. Moreover, a non-negligible part of the pollution (about $20\,\mu g/m^3$ obtained at Mast 6, see Fig. 4), also reaches the first floor window of the building (see Fig. 3). Indeed, Fig. 4 shows that the concentration at Mast 2 (on the building sidewalk) is 20 times higher than the one at Mast 1 (near the two houses). Even on the building sidewalk, the pollutant concentration varies significantly, *i.e.* from $10\,\mu g/m^3$ to $60\,\mu g/m^3$ according to the spatial position (see Masts 2, 3 and 4).

To sum up, high concentrations are observed obviously at the source position, at the vicinity of the building on the sidewalk and at the first floor building window.

3.3. Determination of high-polluted areas and definition of quantities of interest

From the pollution maps in Sense-City (Fig. 3), two critical pollution areas are selected :

- The first area is located on the sidewalk near the concrete building and is defined by the subdomain

$$\Omega_{q1} = \{x \in [-5\mathrm{m}, 5\mathrm{m}],\ y \in [-5.5\mathrm{m}, -4\mathrm{m}],\ z \in [1\mathrm{m}, 2\mathrm{m}]\}$$

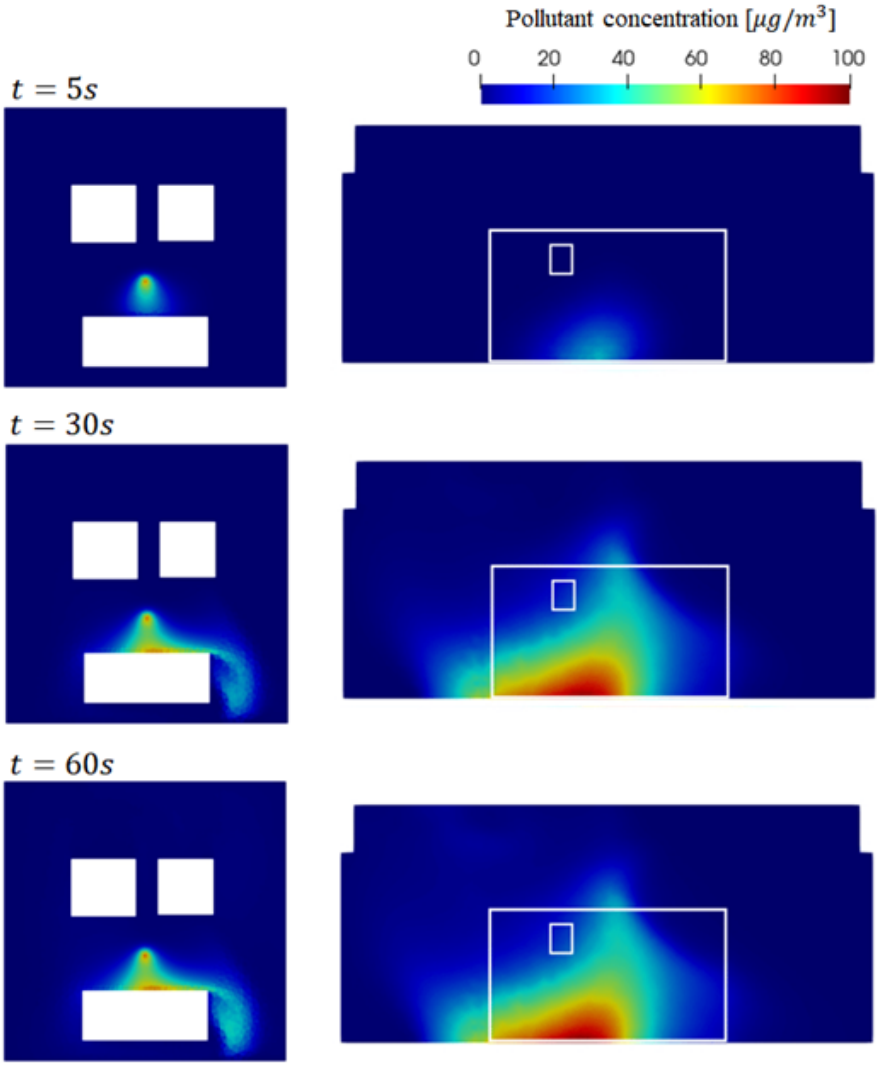

Figure 3: Spatial pollution maps ($\mu g/m^3$) for Sc = 0.7 as a function of time, in the x-y plane at z = 1.5m (left) and in the x-z plane at y = −5.4m (right). The white rectangular contour represents the building and the window of the first floor.

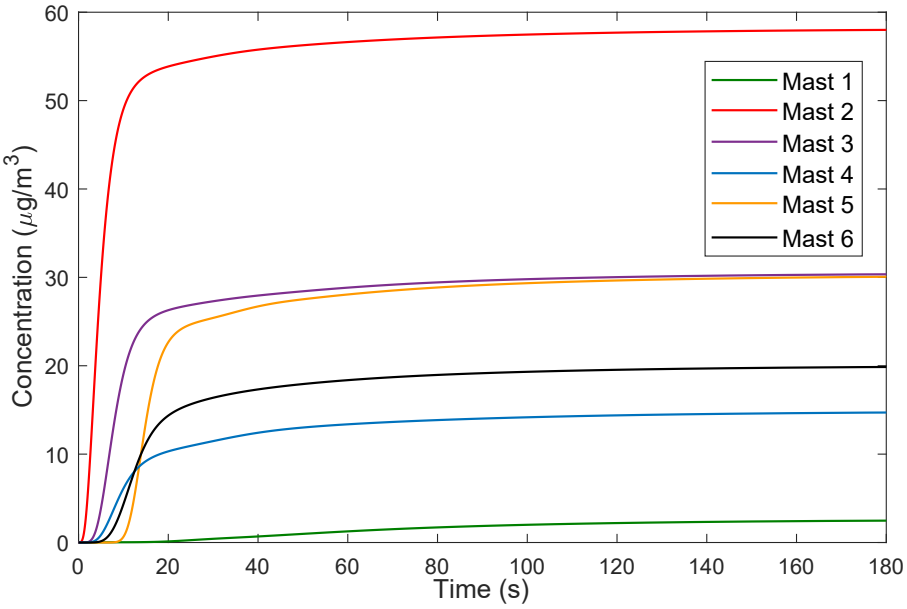

Figure 4: Pollutant concentration from simulation at the masts of Sense-City district as a function of time - no depolluting panels.

.

- The second area corresponds to the vicinity of the first floor building window and is defined by the subdomain

$$\Omega_{q2} = \{x \in [1.5\text{m}, 2.5\text{m}],\ y \in [-5.5\text{m}, -5.3\text{m}],\ z \in [3.7\text{m}, 5\text{m}]\}$$

For each high-polluted area, we define a quantity of interest $\mathcal{J}_i,\ i \in \{1, 2\}$ (see Eq. (4)) associated to the spatial-averaged concentration over the whole time interval $[0, 180s]$. Hence, the space function $f_{q_i}(\mathbf{x}),\ i \in \{1, 2\}$ used to extract the averaged concentration in the critical areas $\Omega_{q_i},\ i \in \{1, 2\}$ in Eq. (4) is given by

$$f_{q_i}(\mathbf{x}) = \begin{cases} 1/|\Omega_{q_i}| & \text{for } \mathbf{x} \in \Omega_{q_i} \\ 0 & \text{elsewhere} \end{cases} . \tag{13}$$

and the time function for both quantities of interest is $\xi(t) = 1/T$ on the whole time interval $[0, T = 180s]$.
The numerical estimation of the two quantities of interest, in the configura-

tion without depolluting panels, are:

$$\begin{cases} \mathcal{J}_1 = 33.0 \ \mu g/m^3 \\ \mathcal{J}_2 = 17.9 \ \mu g/m^3 \end{cases} \tag{14}$$

3.4. Smart placement of depolluting panels to improve air quality in high-polluted areas

Once the quantities of interest $\mathcal{J}_i, i \in \{1, 2\}$ are set, the adjoint problem (see Eq. (8)) is solved. Fig. 5 shows the adjoint concentration on the surfaces of the domain associated to the quantity of interest $\mathcal{J}_2$ (*i.e.* the mean value of the pollutant concentration at the building window). Let us recall that the adjoint solution corresponds to a sensitivity function as regards of the chosen quantity of interest. Thus, if the adjoint solution is almost null in a part of the domain, it means that actions in this part of the domain, like emissions of pollutants or placement of depolluting panels, will have no influence on the considered quantity of interest.

To select the best depolluting panels location for improving the chosen quantities of interest, the spatial sensitivity indicators defined by Eq. (10) are computed on all the wall surfaces of the domain ($\Gamma_p = \Gamma_w$). In Fig. 6, the sensitivity indicator maps are shown for the two selected quantities of interest: mean pollutant concentration values on the building sidewalk ($\mathcal{J}_1$) and at the building window ($\mathcal{J}_2$). Each indicator $I_i, i \in \{1, 2\}$ is the result of the product of the pollutant concentration field C (direct concentration) and the adjoint state $\tilde{C}_i$ associated to each $\mathcal{J}_i$. Hence, the depolluting panels are to be positioned in areas where both direct and adjoint concentrations are high. The maximum value of the sensitivity indicator I_1 is about 25 whereas the value of I_2 can exceed 50. It means that installing a limited surface in m^2 of depolluting panels in the most sensitive areas can have a bigger impact on the decrease of the pollutant concentration at the building window ($\mathcal{J}_2$) than the one at the building sidewalk ($\mathcal{J}_1$). From Fig. 6, it can be noted that depolluting panels have to be positioned on the bottom of the building surface, and on a restricted part of the sidewalk and on the road to reduce the quantity of interest $\mathcal{J}_1$ (sidewalk pollutant concentration). Concerning the pollutant concentration at the building window $\mathcal{J}_2$, air pollution exposures can be decreased by placing panels below the window on the building facade, on a portion of the sidewalk and on the road.

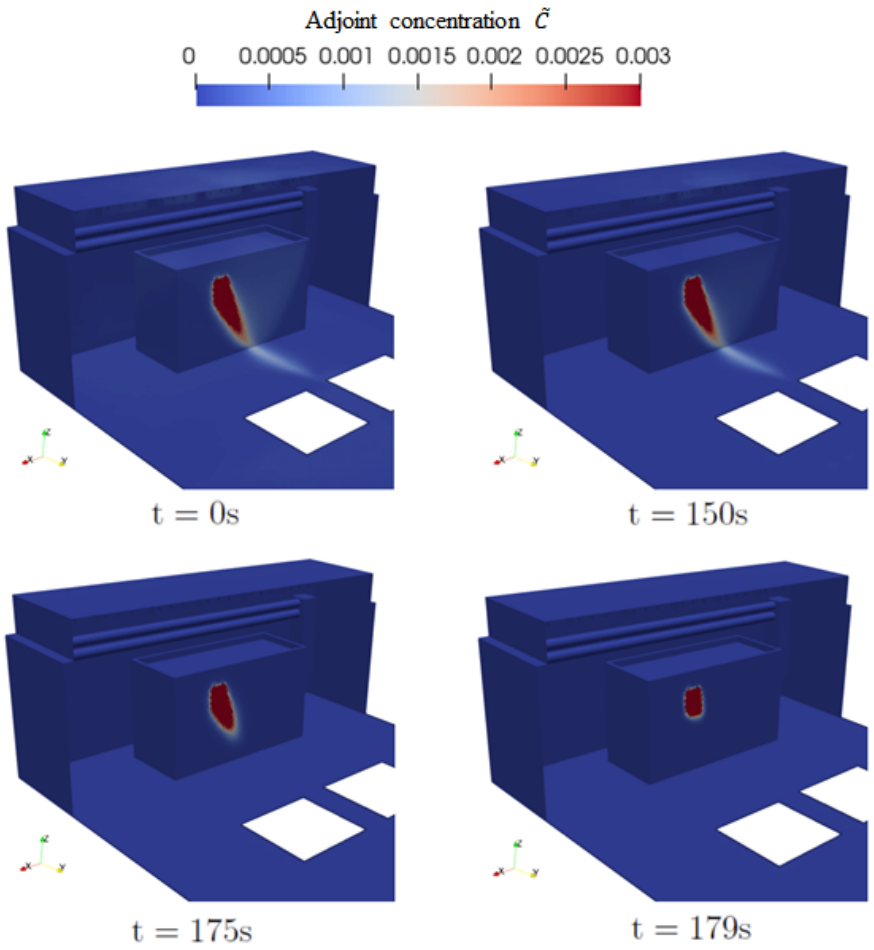

Figure 5: Adjoint solution $[m^{-3}]$ represented at the surfaces of Sense-City district - Quantity of interest $\mathcal{J}_2$ associated to the pollutant concentration at the vicinity of the window building.

.

In Fig. 7, the two sensitivity indicators I_1 and I_2 are displayed on the most influential surfaces, *i.e.* the building walls, the building sidewalk, and the road. Three areas to install depolluting panel, noted DP1, DP2, and DP3, are determined by taking the sensitivity threshold value to 5. Let us note that the lower the sensitivity threshold value, the larger the panel deployment area. In practice, the threshold value can be chosen to get a deployment

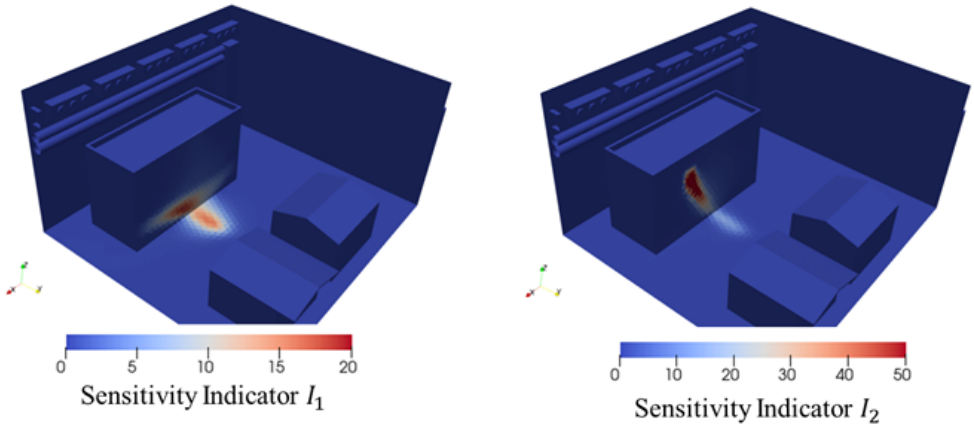

Figure 6: Sensitivity indicator maps I_1 associated to the pollutant concentration at the building sidewalk $\mathcal{J}_1$ (at left) and I_2 associated to the pollutant concentration at the building window $\mathcal{J}_2$.

.

surface of panels strictly less than the maximum deployment surface allowed by the urban planner. In the Sense-City application, the total surface of depolluting panels corresponds to $29.7m^2$. Let us explain in more detail the three optimal depolluting areas represented in Fig. 7. Firstly, for operational urban purposes, rectangular areas are preferred to more complex shapes.

- "DP1" surface is located on the building wall above the window, and its coordinates are $\{x \in [-0.3\text{m}, 2.7\text{m}], y = -5.5\text{m}, z \in [2\text{m}, 3.7\text{m}]\}$. As shown in Fig. 6, panels in "DP1" allow mainly to improve the air quality at the building window and thus to reduce outdoor/indoor transfer of pollutants;

- "DP2" surface is located on the bottom building wall, and its coordinates are $\{x \in [-3.4\text{m}, 4\text{m}], y = -5.5\text{m}, z \in [0\text{m}, 2\text{m}]\}$. Panels in this area contribute to improving both quantities of interest $\mathcal{J}_1$ and $\mathcal{J}_2$;

- "DP3" surface is placed on a part of the sidewalk and the road, and its coordinates are $\{x \in [-1.9\text{m}, 1.3\text{m}], y \in [-2.5\text{m}, -5.5\text{m}], z = 0\text{m}\}$. As with the panels in "DP2" area, the one in "DP3" surface can reduce the pollutant concentrations on the building sidewalk and window.

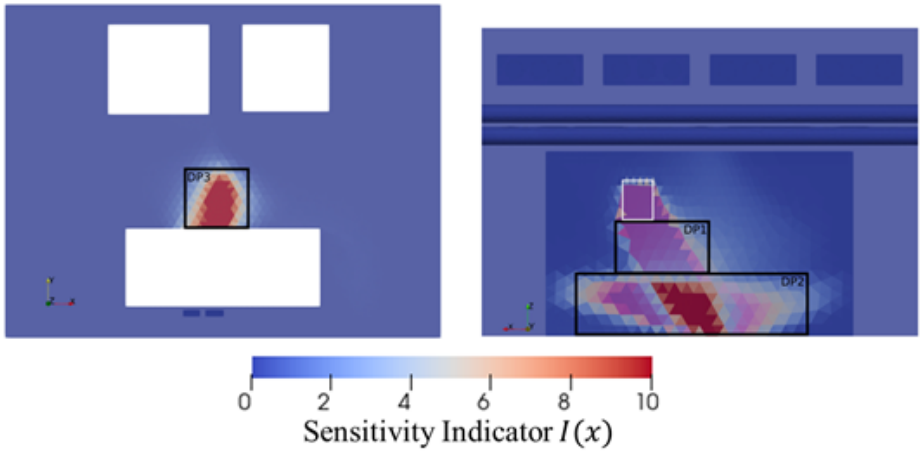

Figure 7: Representation of smart placement of depolluting panels (indicated by black rectangles) in Sense-City district on the road and the sidewalk (at left) and on the building facade (at right) to improve the quantities of interest $\mathcal{J}_1$ and $\mathcal{J}_2$ - White rectangular denotes the window position.

.

3.5. Numerical validation of the optimized placement of depolluting panels

In Section 3.4, the smart placement of depolluting panels to improve both quantities of interest $\mathcal{J}_1$ and $\mathcal{J}_2$ is determined using the spatial sensitivity indicator defined in Eq. (10). To validate numerically the relevance of the predicted position of panels, the pollutant concentration in Sense-City district and the quantities of interest are evaluated by solving the advection-diffusion direct problem (see Eq. (5)) in three different configurations:

- "no depollution case" - it corresponds to the initial district urban planning, *i.e.* in the absence of depolluting device. It was detailed in Sections 3.2 and 3.3;
- "optimal depollution placement" - the depolluting panels DP1, DP2 and DP3, determined from the smart placement strategy in Section 3.4, are integrated in the Sense-City district;
- "bad depollution placement" - depolluting panels are massively deployed on all the district roads (see Fig. 2) except in the sensitive area DP3.

For these three urban planning configurations, the quantities of interest $\mathcal{J}_1$ (mean pollutant concentration at the building sidewalk) and $\mathcal{J}_2$ (mean concentration at the building window) are calculated. The numerical results are summarized in Table 1. In the case of "optimal depolluting panels placement", different values of the reaction rate k are investigated for all the panels DP1, DP2, and DP3. If the reaction rate k of the depolluting panels is less or equal to $0.01m/s$, the reduction of the pollutant concentration in the areas of interest is not significant, *i.e.* less than 2 $\mu g/m^3$. As predicted from the sensitivity indicator in Fig. 6, the smart placement of depolluting panels may have more impact on the improvement of the air quality at the building window ($\mathcal{J}_2$) than the one on the building sidewalk ($\mathcal{J}_1$). Table 1 confirms this expectation. Indeed, when considering depolluting panels (DP1,DP2,DP3) with $k = 1m/s$, the quantity of interest $\mathcal{J}_2$ decreases by about 10 $\mu g/m^3$ (-59% variation) whereas for $\mathcal{J}_1$ the decrease is less than 5 $\mu g/m^3$ (-14% variation). According to the study of the airflow in the Sense-City district (Streichenberger et al., 2021), the pollutant may pass closer to the district surfaces (road, sidewalk, and building surfaces) on the trajectory between the source of pollution and the building window than the one between the source and the sidewalk. In summary, the depolluting panel strategy will not be efficient if the pollutant does not pass close to district surfaces.

In the last configuration noted as "bad depollution placement", the panels are largely deployed on all the road surfaces of the Sense-City district except the area DP3. Hence, it represents $172m^2$ of depolluting panels over a total ground surface of $328m^2$. Even for a high value of depolluting panel reaction rate k, *i.e.* $k = 1m/s$, Table 1 shows that a massive deployment of panels can result in no improvement of the air quality in the areas of interest when the panels are badly positioned. In conclusion, the use of urban airflow in numerical strategies can allow the design of efficient urban planning with a limited surface area of depolluting panels to improve the air quality in critical areas.

4. Real case application - Paris district

In Section 3, the numerical strategy for smart placement of depolluting panels was applied in a simple urban geometry and under controlled weather conditions in Sense-City to demonstrate its effectiveness. In this section, the use of the numerical strategy is extended to a real urban district of Paris

Configuration		$\mathcal{J}_1$ ($\mu g/m^3$)	$\mathcal{J}_2$ ($\mu g/m^3$)
Panel placement	$k(m/s)$		
"No depolluting panel"	-	33.0	17.9
"Optimal depolluting panel placement"	0.01	32.5	16.6
	0.1	30.4	11.4
	1	28.3	7.3
"Bad depolluting placement"	1	33.0	17.9

Table 1: Numerical values of the quantities of interest in different urban planning configurations for Sense-City district, k denotes the reaction rate of the depolluting panels.

with realistic wind conditions. Realistic weather conditions and pollution situations considered here, represent the two most dominant wind directions encountered in Paris and actual measured NO_x pollutant concentrations on the roads. In Paris region, generally, the two dominant airflows are North-East (NE) and South-West (SW). Thanks to the cooperation with Airparif agency, two critical days and specific hours are determined, corresponding to high pollutant levels and NE or SW wind conditions. Accordingly, the 4^{th} of December 2021 at 7 pm with a wind direction of 230 degrees and the 16^{th} of December 2021 at 11 am with a 70 degrees wind direction are selected. These two studied winter days are outside of the intensive photochemical period (April-September).

4.1. Computational setting

The direct simulation for flow and pollutant dispersion is performed with the finite-volume CFD software "Code_Saturne"(Frederic et al., 2004). In order to compromise between accuracy and computational cost, the pseudo-steady-state incompressible Reynolds-Averaged Navier-Stokes (RANS) with $K-\omega\ SST$ turbulence model is considered. It was also used in Sense-City flow simulation (Streichenberger et al., 2021). Second-order upwind schemes are chosen to compute velocity, turbulence kinetic energy, and specific dissipation. As in Sense-City case, the turbulent Schmidt number Sc_t is fixed at 0.7.

OpenFOAM (Greenshields et al., 2015) (open source software) is used to solve the pseudo-steady-state adjoint advection-diffusion equation, which corresponds to Eq. (8) without the time derivative term. A first-order upwind scheme is chosen to discretize the advection term.

4.2. From real urban geometry to mesh generation

The study area is a part of the 8th arrondissement of Paris (France), which is located on the west side of the city (see Fig. 8 (a)). This area includes housing, business, political activities, and many tourist spots, such as the Avenue des Champs-Élysées. The white zone in Fig. 8 (b) indicates the main domain of focus in this study. To imitate an actual incoming flow affected by windward buildings, the extra regions represented with yellow lines in Fig. 8 (b) are added. The domain size is about 2 km in the NS direction and 1.55 km in the EW direction. An air quality measurement station of the Airparif agency is present in the studied domain at the Avenue des Champs-Élysées (see red circle in Fig. 8 (b)). Many streets in this area are known to be highly polluted because of the traffic, *e.g.* Av des Champs-Élysées, Bd Malesherbes, and Rue de Miromesnil.

Figure 8: (a) Area of simulation: overall view of Paris (at left) and (b) detail view of the study area (at right).

The numerical mock-up of the urban area is generated *via* a software

chain. From IGNMap, 2D shapes with height information of each building are exported. Then, 3D geometry is obtained by the automatic extrusion process of each building in CityEngine software. Let us note that precise heights of the buildings and courtyards are taken into account in the main domain of interest (white zone in Fig. 8) whereas geometrical simplifications are made in the *extra* region (yellow line in Fig. 8) such as constant height of buildings and removal of courtyards. Lastly, an unstructured mesh of the computational domain is generated in SALOME software (Ribes and Caremoli, 2007). The computational domain is adapted according to the wind direction. Fig. 9 shows the computational domain and mesh when considering wind from the SW direction. For NE case, only the building geometries are rotated to make a new computational domain. The distances from the outer edges of the building geometries to the domain boundaries are as follows: about $5H_{max}$ (H_{max} is equal to 42.5 m, the maximum building height in the considered domain) from the inlet boundary, approximately $8H_{max}$ from the lateral boundaries, exceeding $20H_{max}$ from the outlet boundary, and more than $10H_{max}$ from the top boundary. These distances meet the recommendations outlined in the guidebook (Architectural Institute of Japan, 2020). As mentioned, the wind direction, the days, and the time chosen for the simulations are 230 degrees on 4^{th} December 2021 at 7 pm (SW) and 70 degrees on 16^{th} December 2021 at 11 am (NE). The number of cells is about 25 million for SW and NW cases. In the studied domain, 1m mesh size is used where traffic pollutant sources are put, and 3m mesh size elsewhere.

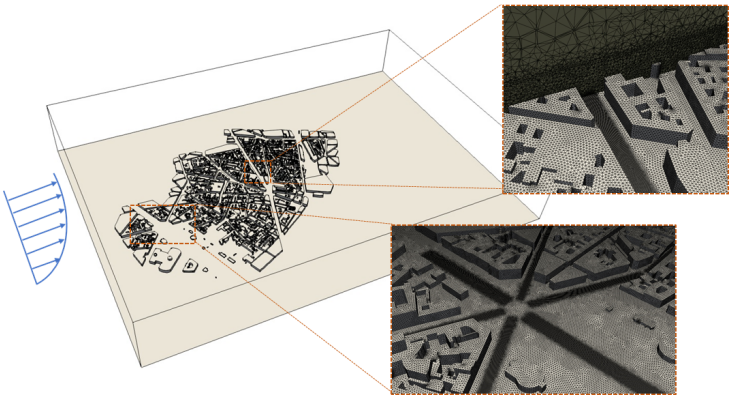

Figure 9: Computational area and mesh of simulation for Paris SW case.

4.3. Boundary conditions and traffic pollutant source

At the inlet faces, as shown in Eqs. (15-17), a logarithmic profile for velocity, a constant value for kinematic energy and a height-dependent profile for specific dissipation are imposed (P.J. Richards, 2011).

$$U = \frac{u_*}{\kappa} \ln\left(\frac{z + z_0}{z_0}\right) \tag{15}$$

$$\mathrm{k} = \frac{{u_*}^2}{\sqrt{C_\mu}} \tag{16}$$

$$\omega = \frac{u_*}{\sqrt{\beta'}\kappa_{\mathrm{k}-\omega} z} \tag{17}$$

where u_*, z_0, and κ are the friction velocity, the roughness length, and Von Karman constant. The roughness length is taken to 1 m, u_* are 2 m/s for SW and 2.5 m/s for NE cases. The details of the other coefficients C_μ, β' and $\kappa_{\mathrm{k}-\omega}$ can be found in (P.J. Richards, 2011). On the outlet face, zero-gradient condition is imposed. Wall function is used on the bottom face and all the building surfaces. Symmetry conditions are given on laterals and upper faces.

Concerning NO_x emissions from traffic, they are estimated on one-hour intervals by the Airparif agency using emission factors from COPERT (Ntziachristos et al., 2009) and data assimilation, which combines observed data and a traffic model. In the present computational domain, 44 main roads, which contribute the most to traffic pollution, are considered as pollutant sources (see red lines in Fig. 10). In the CFD calculations, the pollutant sources on the main roads are modeled as volumetric source terms in the advection-diffusion equation. The pollutant volumetric sources are defined on the width of the roads from 0 m to 1 m height to mimic traffic emissions with a one-hour average pollutant concentration. NO_x emissions on each street are given in $\mu g/m^3/s$. For the details of the NOx values, see Appendix B.

4.4. Simplifications and limitations of Paris study case

The main assumptions made to simplify the Paris study case in terms of geometry, airflow, pollutant dispersion, and chemical modeling are listed and summarized in this section.

Figure 10: Position of main traffic pollutant sources (44 roads in the considered domain).

.

- *Wind and traffic pollution scenarios*: the airflow and the traffic pollutant dispersion in the Paris case are studied on hourly-averaged time intervals using pseudo-steady simulations. Only two characteristic study cases, *i.e.* highly-polluted periods from traffic (morning and evening) with Paris region dominant winds (South-West and North-East), are analyzed to propose first recommendations on the placement of depolluting panels in the urban area;

- *Estimated traffic pollution emission*: as mentioned in Section 4.3, the pollutant sources are estimated from a traffic model and pollutant emission factors. The fleet and the velocity of the vehicles not being well-known, these input data are subject to uncertainties;

- *No height variation in the geometry*: in the present Paris domain, the elevation is about 20 m lower from north to south. Although the topography can influence the airflow, herein the slope being slight, the height variation of the terrain is not considered;

- *Airflow disturbance induced by urban equipment, trees, traffic, and temperature*: trees and vehicles can increase turbulence and air mixing in urban areas. Thereby, they may facilitate the dispersion of pollutants

and reducing pollutant concentrations. However, for simplicity, they are not considered in this case study. In the same way, some geometrical details, such as urban equipment, are not included in the digital twin. Furthermore, the buoyancy effects caused by temperature-induced density changes and the atmospheric stability caused by temperature differences between the ground and the atmosphere are not considered;

- *Chemical reaction of traffic pollutants*: from NOx traffic emissions provided by AirParif agency, NOx background concentration, and the detailed airflow numerical fields, the cartography of NOx concentration in the Paris domain is computed using advection-diffusion PDE. The possible reactions with other chemical species are not taken into consideration. Herein, the depolluting action of the panel surface is simply modeled by boundary conditions with a first-order reaction. Its reaction rate function k is assumed to be independent of UV radiation levels and air temperature;

- *Photochemical reactions in urban environment*: when reactive pollutants are exposed to UV radiation, photochemical reactions occur and can significantly impact urban air quality. However, these phenomena are not considered in our approach. Therefore, the proposed method should be applied outside of the intensive photochemical period, such as in winter;

- *Simulation settings*: certain CFD model parameters such as the roughness length and the Schmidt number are fixed in the study to given numerical values. The chosen values can have an impact on the recommended placement of depolluting panels.

4.5. Cartography of the pollutant concentration and critical pollution areas in Paris

The first step of the proposed numerical strategy is to make a cartography of pollutant concentration. Fig. 11 shows the mean velocity and NOx concentration at 1.5 m height for the SW and NE cases. Concerning the numerical estimation of NOx concentrations, measurement values of the air

		($\mu g/m^3$)
	SW	NE
Background concentration at *Chatelet-Les Halles* station	45.5	164.5
CFD simulation (traffic-derived emission)	52.3	5.4
Total predicted concentration (background + CFD)	97.8	169.9
Measurement station at Av des Champs-Elysées	123.0	154.1

Table 2: Comparison of NOx concentration between CFD and measurement station.

quality subway station *Chatelet-Les Halles* [2] (in the center of Paris) are used as background concentrations: 45.5 μg/m^3 and 164.5 μg/m^3 for SW and NE cases, respectively. CFD is used to compute the cartography of NOx concentration resulting from traffic emissions. Hence, the total NOx concentration is obtained by adding the background concentration to the traffic-derived concentration predicted by CFD. In Table 2, the numerical NOx concentration is compared with the measured concentration at the air quality station of AirParif agency located at Av des Champs-Élysées (see red circle in Fig. 8). The traffic-derived pollutant concentration at the air quality station is lower for NE wind direction case than for SW wind. In fact, few traffic emissions are conveyed to the measurement station as (i) the wind direction is NE, (ii) the air quality station is placed on the NE sidewalk of Champs Elysées and (iii) an important green park is present at the vicinity of the air quality station in the NE direction (no big traffic emission). On the contrary, in the SW case, the measurement station observes the high traffic pollutant emission from Av des Champs Elysées. Overall, in both simulated cases, an acceptable gap, *i.e.* less than 25%, is obtained between the simulated and measured NOx concentrations at Av des Champs-Élysées. Nevertheless, it is important to note that herein the comparison is based on results from just one local measurement station. This does not provide a comprehensive assessment of accuracy over the entire computational domain, meaning there might be errors in other areas. However, it is challenging to verify overall accuracy since the number of measurement stations is usually limited within real urban areas.

[2] Since this station is far from any large street, the measured concentration is considered as a background concentration by AirParif.

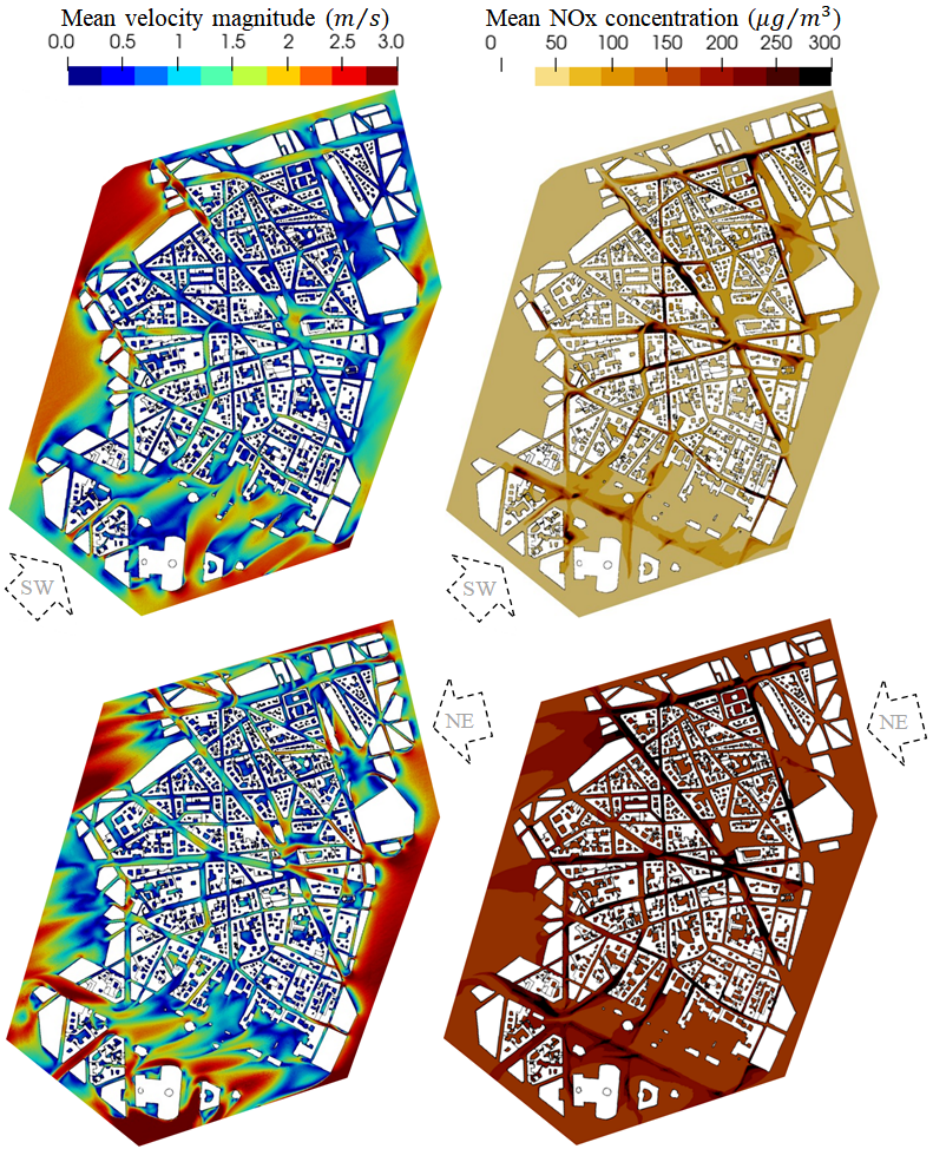

Figure 11: Mean velocity and not Mean NOx concentration on 1 hour-interval at 1.5 m height: SW case (top) and NE case (bottom).

.

CFD results represented in Fig. 11 highlight that the pollutant concentration is inhomogeneous at the district and street levels. As expected, high

pollutant concentrations are predicted on the 44 main streets where volumic sources are placed (e.g. Av des Champs-Élysées and Bd Malesherbes). Low airflow velocities in some areas result in pollution accumulations such as in Rue de Miromesnil. Moreover, it is observed on many streets that the pollutant concentrations are high only on one side. This is due to the typical pollutant distribution of the street canyon where the highest concentrations are noticed on the leeward side of roads, as the street primary vortex (Dabberdt et al., 1973) conveys pollutants leeward. For example, Fig. 12 shows pollutant concentration and wind direction on a street's cross section at 58 Bd Malesherbes for the SW case. On the left side (leeward), the NOx concentration is higher than the right side and above 500 $\mu g/m^3$ at the pedestrian level, with decreasing concentration as height increases. Let us note that due to the simplification assumptions considered and detailed in Section 4.4, the predicted NOx concentration may give over-estimation.

The next step is to select critically polluted areas (areas of interest) where the air quality should be improved. As regards the two wind direction cases, four areas of interest are selected from the NOx pollutant cartographies:

- Ω_{q1}: southwest sidewalk from 69 to 85 Bd Malesherbes represented in Fig. 13 (a) in red, and in Fig. 14 (a) for SW case. Dimension of the area is 5 m width, 140 m length, and height belongs to $[0.5\text{ m}, 2\text{ m}]$. The associated mean pollutant concentration $\mathcal{J}_1$ is 627 $\mu g/m^3$.

- Ω_{q2}: building facade of the lower floors on the southwest side from 69 to 81 Bd Malesherbes represented in Fig. 13 (a) in blue and in Fig. 14 (a) for SW case. The dimension of the area is 0.5 m width, 110 m length, and height belongs to $[4\text{ m}, 9.2\text{ m}]$. The associated mean NOx concentration $\mathcal{J}_2$ is 427 $\mu g/m^3$.

- Ω_{q3}: sidewalks at the intersection of Rue de Miromesnil and Rue la Boétie represented in Fig. 13 (b) and in Fig. 14 (b)) for SW case. The dimension of the area is $1 \sim 2.5$ m width, $20 \sim 50$ m length, and height belongs to $[0.5\text{ m}, 2\text{ m}]$. The associated mean NOx concentration $\mathcal{J}_3$ is 252 $\mu g/m^3$.

- Ω_{q4}: north-east sidewalk from 48 to 60 Bd Malesherbes represented in Fig. 13 (c) and in Fig. 14 (a) for NE case. Dimension of the area

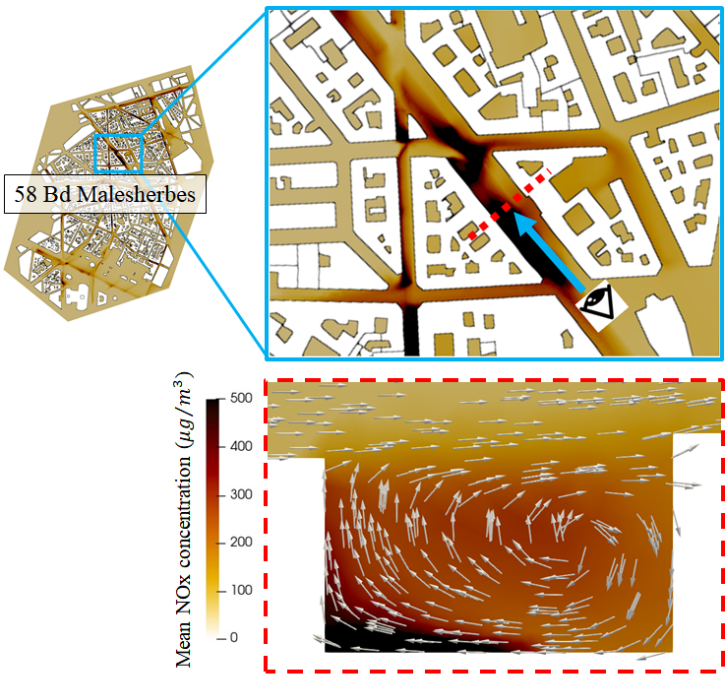

Figure 12: Mean NOx concentration and wind direction on the vertical direction in SW case at 58 Bd Malesherbes.

.

is 4 m width, 140 m length, and height belongs to $[0.5\text{ m}, 2\text{ m}]$. The associated mean NOx concentration $\mathcal{J}_4$ is 326 $\mu g/m^3$.

The quantities of interest $\mathcal{J}_1$, $\mathcal{J}_3$ and $\mathcal{J}_4$ have been selected in order to improve the air quality on sidewalks frequented by pedestrians. $\mathcal{J}_3$ is also of particular interest as it is located at a road intersection having the crowded metro station entrance "Miromesnil" and many city shops. Lastly, reducing air pollution on the building facade, *e.g.* $\mathcal{J}_2$ at Bd Malesherbes, is important in order to decrease the transfer of traffic pollutants from the outdoors to the indoors.

4.6. Adjoint solution and smart placement of depolluting panels in Paris

To smartly place the depolluting panels on the surfaces of the urban domain, the last step is to calculate the adjoint concentration and the sensitivity indicator for each selected quantity of interest defined in the previous

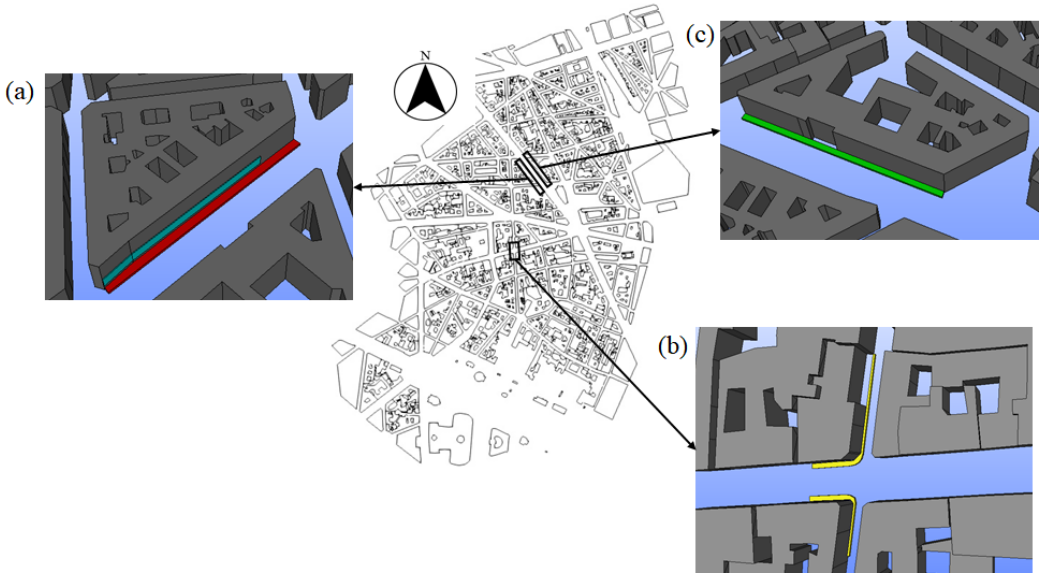

Figure 13: Selected areas of interest in the Paris district where air quality should be improved: (a) the south-west sidewalk in red and the lower floors of the building facade in blue from 69 to 81 Bd Malesherbes, (b) sidewalks at the intersection of Rue de Miromesnil and Rue de Boétie, (c) the north-east sidewalk from 48 to 60 Bd Malesherbes.

section. As explained before, the sensitivity indicator becomes significant when both direct and adjoint concentrations are high. Fig. 15 shows the cartographies of the NOx concentration (solution of the direct problem), the adjoint concentration, and the resulting sensitivity indicator on the surfaces of the domain for each quantity of interest. The bold yellow lines in the sensitivity indicator map denote the contour lines of the sensitivity indicator at 0.1 for both the south-west sidewalk and the lower floor building facade at Bd Malesherbes, at 0.2 at the intersection of Rue de Miromesnil and at 0.003 for the north-east sidewalk at Bd Malesherbes. These values are associated with the chosen sensitivity indicator thresholds. Herein, the thresholds have been selected such that the surface of depolluting panels does not exceed 300 m^2.

On the southwest sidewalk at Bd Malesherbes, let us define the north and south parts of the sidewalk (see Fig. 16). Firstly, concerning the quantity of interest $\mathcal{J}_1$, the highest sensitivity indicator values can be seen on the ground of the north part. It corresponds to a part of the sidewalk, of the road and

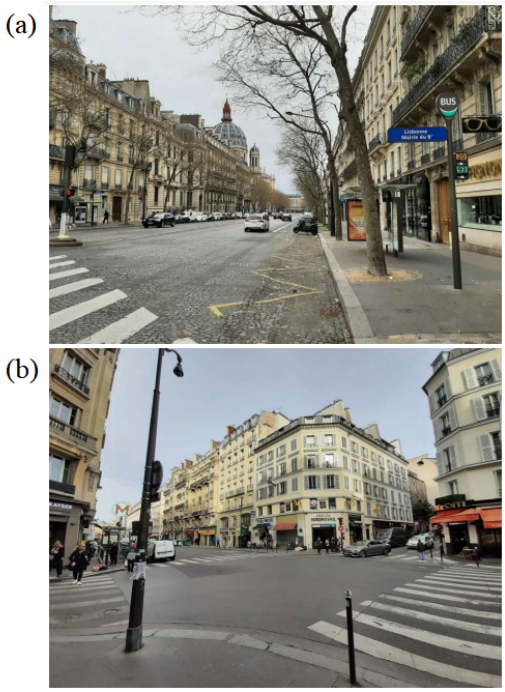

Figure 14: Pictures of the areas of interest in the Paris district: (a) 58 Bd Malesherbes and (b) 43 Rue de Miromesnil.

.

of the lower floor's building facade (Fig. 15 (a)). Similarly, for the quantity of interest $\mathcal{J}_2$, significant sensitivity indicator values are mainly located on the north part of Bd Malesherbes on the lower floor building facade (Fig. 15 (b)). In the other regions, the indicator is relatively low. For $\mathcal{J}_1$ and $\mathcal{J}_2$, variation of the sensitivity indicators are found, even on the same sidewalk and building facade, which are attributed to the magnitude of adjoint concentration. Looking at the airflow characteristics in Bd Malesherbes (Fig. 16), a typical street canyon flow occurs in the north part. Hence, in the north part of Bd Malesherbes, the pollutant source of the adjoint problem defined on Ω_{q1} and Ω_{q2} are backwardly transported along the ground and building facade by the primary vortex. It leads to high adjoint concentration on the sidewalk, road and building facade in the north part of Bd Malesherbes. On the other hand, in the center and south part (except for the south corner), the adjoint concentration is low on the ground and building facade. In these

areas, the vertical velocity is tiny compared to the north part, and the wind direction near the building surfaces is oriented parallel to the road (Fig. 16). This airflow does not transport the adjoint pollutant concentration near the ground and building facade, resulting in low indicator values in these regions. To sum up, urban airflow plays a major role in the sensitivity indicator level and therefore in determining the smart placement of depolluting panels. The amount of adjoint concentration passing close to the ground or the building surface is a major contributor to the selection of panel location and size.
For the quantity of interest $\mathcal{J}_3$ dealing with the NOx concentration at the street intersection of Rue de Miromesnil and Rue la Boétie, Fig. 15 (c) shows that high sensitivity indicator values are obtained on the sidewalk surfaces, especially in Rue de Miromesnil, a well-known road having heavy traffic, and also on lower floor's building facades. Moreover, the sensitivity indicator is significant at the entrance to the subway station. In this intersection, complex airflow is created as winds come from many directions and merge. Hence, this air mixing favors the direct and adjoint concentrations to reach the ground surfaces and building facades as illustrated.
Concerning the quantity of interest $\mathcal{J}_4$ on the north-east sidewalk of Bd Malesherbes, Fig. 15 (d) indicates very local high sensitivity indicator at the building corner on the south part mainly due to high adjoint concentrations. In addition, a high indicator is obtained around the center of the sidewalk near the vertical setback. (Ng and Chau, 2014) pointed out that vertical setbacks increase airflow and pollutant dispersion in the vertical direction. Its effect contributes to the high adjoint concentration in this region, thereby the high indicator. This finding implies that combining measures to facilitate airflow mixing with depolluting panels can be a more efficient way to improve air quality. However, in this northeast sidewalk case, note that the magnitude of the adjoint concentration and the sensitivity indicator is much smaller than in the other cases. Therefore, putting depolluting panels in the northeast sidewalk can be less efficient.

To conclude, for the improvement of the air quality at Bd Malesherbes (69-85 and 48-60) and at the intersection of Rue de Miromesnil and of Rue la Boétie under the considered wind conditions, the suggested placement of depolluting panels based on the chosen sensitivity contour lines in Fig. 15 are the following:

- Bd Malesherbes - panels should be placed on the north part of the

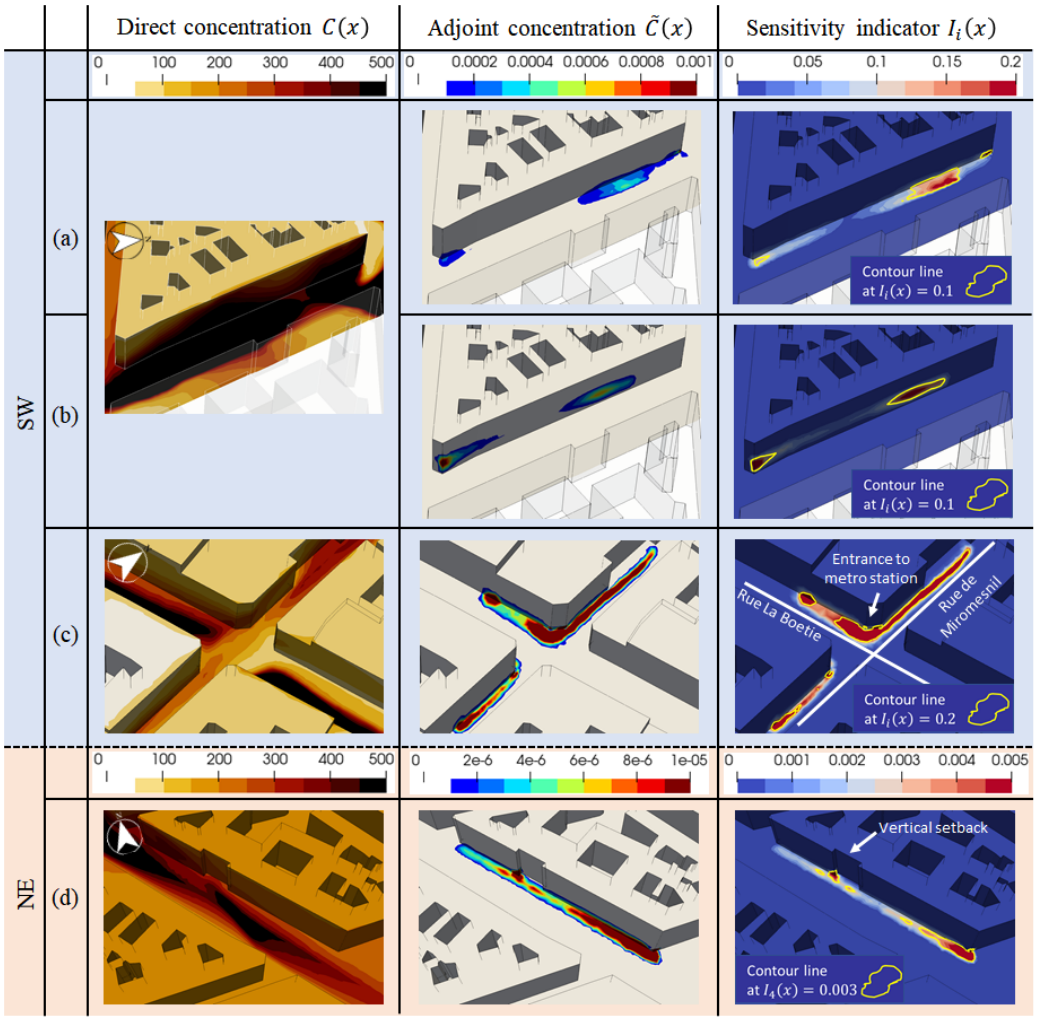

Figure 15: Direct concentration, adjoint concentration, and sensitivity indicator associated with each quantity of interest: (a) the south-west sidewalk from 69 to 85 Bd Malesherbes, (b) the building facade at the lower floor on south-west side from 69 to 81 Bd Malesherbes, (c) the subway station and shops at the intersection of Rue de Miromesnil and Rue la Boétie, (d) the north-east sidewalk from 48 to 60 Bd Malesherbes.

south-west sidewalks (4 m wide $\times$ 30 m long) and of the road adjacent to the sidewalk (3.5 m $\times$ 30 m), on the building facade in the north part (height$\in [2.5\text{m}, 9.5\text{m}]$ $\times$ 35 m) and in the south part (height$\in [2\text{m}, 9\text{m}]$ $\times$ 10 m). Although the placement of panels can be less effective on the

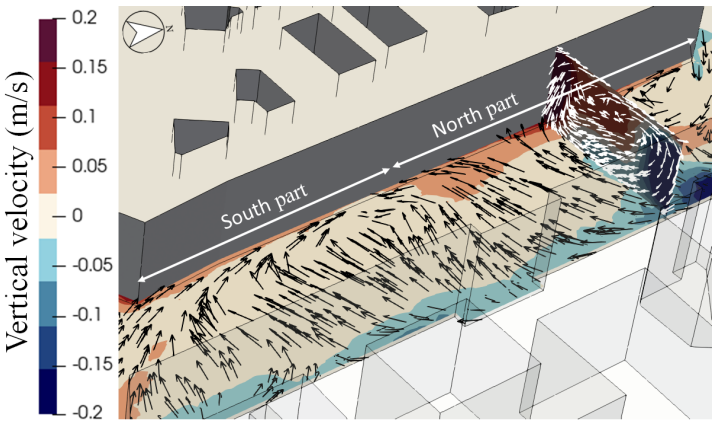

Figure 16: Vertical velocity and wind direction at Bd Malesherbes at 1m height.

.

north-east sidewalk due to the low sensitivity indicator in comparison with the south-west sidewalk, candidate positions are on the sidewalk at the south corner (6 m × 35 m) and in the center of the sidewalk (4 m × 30 m).

- Intersection of Rue de Miromesnil and of Rue la Boétie - panels should be placed on a part of the sidewalk and road on the north side of Rue de Miromesnil (1.5 m wide × 50 m long) and (1.5 m × 50 m) respectively, at the entrance of the metro station (6 m × 15 m) and at the part of the sidewalk on Rue la Boetie (6 m × 5 m). The other candidate position is a part of the south sidewalk on Rue de Miromesnil (1.5 m × 12 m).

The total areas enclosed by each contour line $I_i(x)$ for each quantity of interest are summarized in Table 3. Let us recall that the contour lines of the sensitivity indicators are used as the thresholds to identify the smart placements. In this study, the sensitivity indicator thresholds were chosen empirically for a limited and reasonable deployment of depolluting panels. In practice, the threshold can be chosen depending on how much local authorities want to improve air quality and the cost that can be afforded.

		(m^2)
SW	South-West sidewalk and road at Bd Malesherbes (I_1)	255.7
	South-West building facade at Bd Malesherbes (I_2)	236.2
	Sidewalk and road at the intersection of Rue de Miromesnil (I_3)	252.3
NE	North-East sidewalk at Bd Malesherbes (I_4)	239.6

Table 3: Area of depolluting panel enclosed by $I_1(x) = 0.1$, $I_2(x) = 0.1$, $I_3(x) = 0.2$ and $I_4(x) = 0.003$.

5. Conclusions and perspectives

The goal of this article was to propose a simple and preliminary operational numerical strategy for a smart deployment of depolluting panels in urban areas. These panels can adsorb and degrade a part of traffic pollutants provided that the pollutants pass near these depolluting surfaces. Hence, we focused on an efficient placement of panels as regards to urban airflows using standard CFD models and adjoint formulation. The approach can be decomposed into two steps. Firstly, in the diagnosis stage, detailed airflow and pollutant cartographies are computed at the district scale to identify critical highly-polluted areas. The pollutant concentration in these areas are designated as "quantities of interest". Then, in the remediation stage, local sensitivity analysis is performed through an adjoint framework to determine a relevant placement of limited depolluting panels with the aim of reducing the pollutant concentration in localized critical areas. A spatial sensitivity indicator was introduced and computed on all the surfaces of the domain to determine the best placement of depolluting panels. The indicator is the result of the product of the pollutant concentration and the adjoint concentration state. Consequently, the depolluting panels should be deployed on surfaces having high pollutant concentration and significant impact on the chosen quantities of interest (i.e. high adjoint concentration).

The numerical strategy for the optimal placement of depolluting according to urban airflow was applied to two real cases. The first application is a small real-scale district named "Sense-City" under controlled airflow and environmental conditions by way of a huge climatic chamber, with a localized source of pollutants on the road. In the second application, a real district of Paris was studied under two representative wind conditions of the Region Ile

de France and realistic NO_x source emissions given by the Airparif agency. Let us note that only one air quality station was available in the 8th arrondissement of Paris to check the CFD dispersion results, which does not allow a comprehensive assessment of simulation accuracy over the entire computational domain. In both studied cases, highly polluted areas are observed on the sidewalks, roads and building facades. To improve the air quality in these critical areas, the proposed numerical strategy recommends placing depolluting panels on a part of the sidewalks, of the building facades and of the roads adjacent to the sidewalks. By comparing improvement effectiveness in two panel deployment configurations: smart and non-smart placements, it was revealed that a massive aleatory deployment of depolluting panels may not be efficient. Also, it was proved that the urban airflow plays a major role in the sensitivity indicator level and therefore in the efficient placement of depolluting panels. The surface area of depolluting panels can be determined by fixing a threshold value on the sensitivity indicator. In practice, the local authorities can select the threshold value by considering the balance between the level of air quality improvement and the maximum area of depolluting panels (expenditure). Although it was not examined in this study, combinations with other air pollutant mitigation actions, especially those that enhance airflow mixing, may enable the panels to be placed more efficiently.

In the presented results, the first recommendations on depolluting panels placement are essentially given regarding the transport of pollutants via the urban airflows. Herein, many simplifications have been considered for easier practical use. Buoyancy effects, traffic-induced turbulence terms, and tree vegetation are not considered. Moreover, to limit the complexity and the time computation, the pollutant was modeled as passive (multiple pollutant reactions not considered). Lastly, the degradation of the pollutant by the depolluting system is described in a simple way using a boundary condition with a first-order reaction. Despite these simplifying assumptions, the actual proposed method can distinguish "useless panel placement areas" corresponding to surfaces having no impact on the improvement of the quantities of interest and "promising panel placement areas". In future works, a more sophisticated strategy can be developed to take into account the above limitations, to extend to exposure level-based quantities of interest and to get a more precise quantitative evaluation of the "promising panel placement areas". For that, multi-pollutant reactions and multi-physics simulations have to be considered. Indeed, the efficiency of the pollutant degradation based on

photocatalysis depends on the solar irradiance, the temperature, and many other physical parameters. To sum up, coupled models providing notably airflow, solar irradiance, temperature, and pollutant cartographies will allow an improved prediction of panel pollutant degradation and thus an enhanced evaluation of the panel placement. At Université Gustave Eiffel, forthcoming controlled air pollution experiments are to be conducted in the district of the Sense-City equipment to validate the proposed numerical strategy for the smart placement of ZnO depolluting panels.

Acknowledgments

The authors acknowledge the supports from the innovative research project "E3S" funded by Université Gustave Eiffel and Eiffage group and from the project "Sense-City" funded by ANR (France) within the Investment for the Future Program under reference number ANR-10-EQPX-48.

Appendix A. Calculation of Lagrange multipliers and adjoint problem

In Section 2, the constrained minimization problem (6) was rewritten using the Lagrangian $\mathcal{L}$ defined in Eq. (7). After some calculations to find the saddle point of the Lagrangian, we obtain the following relations between the Lagrange multipliers

$$\lambda_2 = -D\nabla\lambda_1 \cdot \vec{\mathbf{n}} - (\vec{\mathbf{v}} \cdot \vec{\mathbf{n}})\lambda_1 \quad \text{on} \quad \Gamma_o \times [0,T] \tag{A.1}$$

$$\lambda_3 = D\lambda_1 \quad \text{on} \quad \Gamma_o \cup \Gamma_n \times [0,T] \tag{A.2}$$

$$\lambda_4 = -\lambda_1 \quad \text{on} \quad \Gamma_p \times [0,T] \tag{A.3}$$

$$\lambda_5 = \lambda_1(t=0) \quad \text{on} \quad \Omega \tag{A.4}$$

and we can show that the Lagrange multiplier λ_1 satisfies

$$\begin{cases} -\dfrac{\partial \lambda_1}{\partial t} - \vec{\mathbf{v}} \cdot \nabla\lambda_1 - div(D\nabla\lambda_1) = f_q\,\xi \quad \text{in} \quad \Omega \times [0,T] \\ \lambda_1 = 0 \quad \text{on} \quad \Gamma_i \times [0,T] \\ \nabla\lambda_1 \cdot \vec{\mathbf{n}} = 0 \quad \text{on} \quad \Gamma_n \times [0,T] \\ -D\nabla\lambda_1 \cdot \vec{\mathbf{n}} = k\lambda_1 \quad \text{on} \quad \Gamma_p \times [0,T] \\ D\nabla\lambda_1 \cdot \vec{\mathbf{n}} + (\vec{\mathbf{v}} \cdot \vec{\mathbf{n}})\,\lambda_1 = 0 \quad \text{on} \quad \Gamma_o \times [0,T] \\ \lambda_1(t=T) = 0 \quad \text{in} \quad \Omega. \end{cases} \tag{A.5}$$

Thus, Eq. (A.5) corresponds to the adjoint problem. By convenience, we note $\tilde{C}(=\lambda_1)$ the solution of this adjoint problem.

Appendix B. NOx road emissions in Paris district

The NOx emission magnitude ($\mu g/m^3/s$) of the 44 roads used in the direct simulation are summarized in Fig. B.17. These data were provided by the Airparif agency. Emission values represent only traffic-derived NOx. These values are given as source terms and are emitted as a constant value of NOx throughout the simulations.

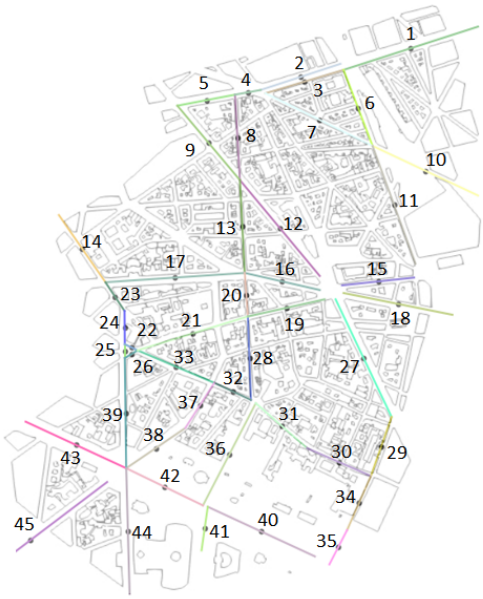

(Unit : $\mu g/m^3/s$)

No. road	SW	NE	No. road	SW	NE
1	17.5	15.6	24	16.9	15.2
2	13.3	17.1	25	8.9	6.5
3	27.2	18.5	26	18.7	21.5
4	20.8	27.7	27	16.5	23.4
5	14.2	18.2	28	8.6	8.4
6	39.7	52.8	29	7.9	11.8
7	11.2	8.4	30	10.6	14.1
8	12.2	20.2	31	10.6	14.1
9	38.8	41.1	32	13.6	31.5
10	11.5	8.9	33	0.7	1.0
11	33.5	34.8	34	10.6	12.3
12	22.1	24.3	35	31.0	41.2
13	20.9	33.7	36	17.7	24.3
14	24.3	43.5	37	11.3	24.8
15	15.5	16.2	38	7.5	16.5
16	12.0	12.6	39	20.2	16.5
17	7.3	5.8	40	13.6	15.4
18	34.4	43.6	41	24.0	35.3
19	19.9	34.2	42	15.5	18.2
20	13.5	10.4	43	21.8	27.7
21	18.4	20.4	44	12.1	18.1
22	9.1	9.6	45	9.9	8.8
23	16.9	15.2			

Figure B.17: Data of NOx emission on 44 roads: position of roads (left) and emission magnitude (right). Note that No.2 and No.3 is summed up and treated as one road.

.

References

An, K., Wong, S.M., Chi-Hung Fung, J., 2019. Exploration of sustainable building morphologies for effective passive pollutant dispersion within compact urban environments. Building and Environment 148, 508–523.

André, M., Pasquier, A., Carteret, M., 2018. Experimental determination of the geographical variations in vehicle fleet composition and consequences for assessing low-emission zones. Transportation Research Part D: Transport and Environment 65, 750–760.

Andre, M., Sartelet, K., Moukhtar, S., Andre, J., Redaelli, M., 2020. Diesel, petrol or electric vehicles: What choices to improve urban air quality in the ile-de-france region? a simulation platform and case study. Atmospheric Environment 241, 117752.

Architectural Institute of Japan, 2020. Guidebook for CFD Predictions of Urban Wind Environment. Architectural Institute of Japan. In Japanese, ISBN:978-4818927186.

Balczo, M., Gromke, C., Ruck, B., 2009. Numerical modeling of flow and pollutant dispersion in street canyons with tree planting. Meteorologische Zeitschrift 18, 197–206.

Bereitschaft, B., Debbage, K., 2013. Urban form, air pollution, and co2 emissions in large us metropolitan areas. The Professional Geographer 65, 612–635.

Bessagnet, B., Menut, L., Curci, G., Hodzic, A., Guillaume, B., Liousse, C., Moukhtar, S., Pun, B., Seigneur, C., Schulz, M., 2008. Regional modeling of carbonaceous aerosols over europe-focus on secondary organic aerosols. Journal of Atmospheric Chemistry 61, 175–202.

Binas, V., Venieri, D., Kotzias, D., Kiriakidis, G., 2017. Modified tio2 based photocatalysts for improved air and health quality. Journal of Materiomics 3, 3–16.

Blocken, B., 2015. Computational Fluid Dynamics for urban physics: Importance, scales, possibilities, limitations and ten tips and tricks towards accurate and reliable simulations. Building and Environment 91, 219–245.

Carruthers, D., Holroyd, R., Hunt, J., Weng, W., Robins, A., Apsley, D., Thompson, D., Smith, F., 1994. Uk-adms: A new approach to modelling dispersion in the earth's atmospheric boundary layer. Journal of Wind Engineering and Industrial Aerodynamics 52, 139–153.

da Silva, F., Costa Reis, N., Santos, J., Goulart, E., de Alvarez, C., 2022. Influence of urban form on air quality: The combined effect of block typology and urban planning indices on city breathability. Science of The Total Environment 814, 152670.

Dabberdt, W.F., Ludwig, F., Johnson Jr, W.B., 1973. Validation and applications of an urban diffusion model for vehicular pollutants. Atmospheric Environment (1967) 7, 603–618.

Darvish, S.M., Ali, A.M., Sani, S.R., 2020. Designed air purifier reactor for photocatalytic degradation of co2 and no2 gases using mwcnt/tio2 thin films under visible light irradiation. Materials Chemistry and Physics 248, 122872.

Derkx, F., Lebental, B., Bourouina, T., Bourquin, F., Cojocaru, C.S., Robine, E., Van Damme, H., 2012. The Sense-City project, in: XVII-Ith Symposium on Vibrations, Shocks and Noise, p. 9p.

Di Sabatino, S., Buccolieri, R., Pulvirenti, B., Britter, R.E., 2008. Flow and pollutant dispersion in street canyons using FLUENT and ADMS-Urban. Environmental Modeling & Assessment 13, 369–381.

Di Sabatino, S., Buccolieri, R., Salizzoni, P., 2013. Recent advancements in numerical modelling of flow and dispersion in urban areas: a short review. International Journal of Environment and Pollution 7 52, 172–191.

Duque, L., Relvas, H., Silveira, C., Ferreira, J., A., M., Gama, C., Rafael, S., Freitas, S., Borrego, C., Miranda, A., 2016. Evaluating strategies to reduce urban air pollution. Atmospheric Environment 127, 196–204.

Elbern, H., Schmidt, H., 2001. Ozone episode analysis by four-dimensional variational chemistry data assimilation. Journal of Geophysical Research: Atmospheres 106, 3569–3590.

Franca, L.P., Frey, S.L., Hughes, T.J., 1992. Stabilized finite element methods: I. application to the advective-diffusive model. Computer Methods in Applied Mechanics and Engineering 95, 253–276.

Frederic, A., Namane, M., Marc, S., 2004. Code saturne: A finite volume code for the computation of turbulent incompressible flows-industrial applications. International Journal on Finite Volumes 1.

Garrido, I., Pastor-Belda, M., Campillo, N., Viñas, P., Yañez, M.J., Vela, N., Navarro, S., Fenoll, J., 2019. Photooxidation of insecticide residues by zno and tio2 coated magnetic nanoparticles under natural sunlight. Journal of Photochemistry and Photobiology A: Chemistry 372, 245–253.

Gousseau, P., Blocken, B., Stathopoulos, T., van Heijst, G.J.F., 2011. CFD simulation of near-field pollutant dispersion on a high-resolution grid: A case study by LES and RANS for a building group in downtown Montreal. Atmospheric Environment 45, 428–438.

Grande, F., Tucci, P., 2016. Titanium dioxide nanoparticles: a risk for human health? Mini reviews in medicinal chemistry 16, 762–769.

Greenshields, C.J., et al., 2015. Openfoam user guide. OpenFOAM Foundation Ltd, version 3, 47.

Gromke, C., Buccolieri, R., Di Sabatino, S., Ruck, B., 2008. Dispersion study in a street canyon with tree planting by means of wind tunnel and numerical investigations - Evaluation of CFD data with experimental data. Atmopheric Environment 42, 8640–8650.

Gromke, C., Jamarkattel, N., Ruck, B., 2016. Influence of roadside hedgerows on air quality in urban street canyons. Atmospheric Environment 139, 75–86.

Hagler, G., Tang, W., Freeman, M., Heist, D., Perry, S., Vette, A., 2011. Model evaluation of roadside barrier impact on near-road air pollution. Atmospheric Environment 45, 2522–2530.

Hammond, J.K.H., Chakir, R., Bourquin, F., Maday, Y., 2019. Pbdw: A non-intrusive reduced basis data assimilation method and its application to an urban dispersion modeling framework. Applied Mathematical Modelling 76, 1–25.

Hang, J., Li, Y., Sandberg, M., 2011. Experimental and numerical studies of flows through and within high-rise building arrays and their link to ventilation strategy. Journal of wind engineering and industrial aerodynamics 99, 1036–1055.

He, D., Li, Y., Wu, J., Yang, Y., An, Q., et al., 2017. Carbon wrapped and doped tio2 mesoporous nanostructure with efficient visible-light photocatalysis for no removal. Applied Surface Science 391, 318–325.

Hecht, F., 2012. New development in freefem++. Journal of Numerical Mathematics 20, 251–265. URL: `https://freefem.org/`.

Hughes, T.J., Mallet, M., Akira, M., 1986. A new finite element formulation for computational fluid dynamics: Ii. beyond supg. Computer methods in applied mechanics and engineering 54, 341–355.

Issakhov, A., Omarova, P., 2021. Modeling and analysis of the effects of barrier height on automobiles emission dispersion. Journal of Cleaner Production 296, 126450.

Koutsourakis, N., Bartzis, J.G., Markatos, N.C., 2012. Evaluation of Reynolds stress, k-epsilon and RNG k-epsilon turbulence models in street canyon flows using various experimental datasets. Environmental Fluid Mechanics 12, 379–403.

Le Dimet, F.X., Talagrand, O., 1986. Variational algorithms for analysis and assimilation of meteorological observations: theoretical aspects. Tellus A 38A, 97–110.

Le Pivert, M., Kerivel, O., Zerelli, B., Leprince-Wang, Y., 2021. Zno nanostructures based innovative photocatalytic road for air purification. Journal of Cleaner Production 318, 128447.

Le Pivert, M., Zerelli, B., Martin, N., Capochichi-Gnambodoe, M., Leprince-Wang, Y., 2020. Smart zno decorated optimized engineering materials for water purification under natural sunlight. Construction and Building Materials 257, 119592.

Leung, D.Y., 2015. Outdoor-indoor air pollution in urban environment: challenges and opportunity. Frontiers in Environmental Science 2, 69.

Li, X.X., Liu, C.H., Leung, D.Y.C., Lam, K.M., 2006. Recent progress in CFD modelling of wind field and pollutant transport in street canyons. Atmospheric Environment 40, 5640–5658.

Meng, X., Liu, C., Chen, R., Sera, F., Vicedo-Cabrera, A., Milojevic, A., Guo, Y., Tong, S., Coelho, M., Saldiva, P., Lavigne, E., Correa, P., Ortega, N., Osorio, S., Kyselý, J., Urban, A., Orru, H., Maasikmets, M., Jaakkola, J., Ryti, N., Huber, V., Schneider, A., Katsouyanni, K., Analitis, A., Hashizume, M., Honda, Y., Ng, C., Nunes, B., Teixeira, J., Holobaca, I., Fratianni, S., Kim, H., Tobias, A., Íñiguez, C., Forsberg, B., Åström, C., Ragettli, M., Guo, Y.L., Pan, S.C., Li, S., Bell, M., Zanobetti, A., Schwartz, J., Wu, T., Gasparrini, A., Kan, H., 2021. Short term associations of ambient nitrogen dioxide with daily total, cardiovascular, and respiratory mortality: multilocation analysis in 398 cities. BMJ-British Medical Journal 372.

Mirzaei, P., Haghighat, F., 2010. A novel approach to enhance outdoor air quality: Pedestrian ventilation system. Building and Environment 45, 1582–1593.

Mishra, D., Goyal, P., 2015. Quantitative assessment of the emitted criteria pollutant in delhi urban area. Aerosol and Air Quality Research 15, 1601–1612.

Mons, V., Margheri, L., Chassaing, J.C., Sagaut, P., 2017. Data assimilation-based reconstruction of urban pollutant release characteristics. Journal of Wind Engineering and Industrial Aerodynamics 169, 232–250.

Ng, W.Y., Chau, C.K., 2014. A modeling investigation of the impact of street and building configurations on personal air pollutant exposure in isolated deep urban canyons. Science of The Total Environment 468-469, 429–448.

Ntziachristos, L., Gkatzoflias, D., Kouridis, C., Samaras, Z., 2009. Copert: A european road transport emission inventory model, in: Information Technologies in Environmental Engineering, Springer Berlin Heidelberg. pp. 491–504.

Peng, C., Li, C., Zou, Z., Shen, S., Sun, D., 2015. Improvement of air quality and thermal environment in an old city district by constructing wind passages. Sustainability 7, 12672–12692.

P.J. Richards, S.N., 2011. Appropriate boundary conditions for computational wind engineering models revisited. Journal of Wind Engineering and Industrial Aerodynamics 99, 257–266.

Pulvirenti, B., Baldazzi, S., Barbano, F., Brattich, E., Di Sabatino, S., 2020. Numerical simulation of air pollution mitigation by means of photocatalytic coatings in real-world street canyons. Building and Environment 186, 107348.

Ramponi, R., Blocken, B., De Coo, L.B., Janssen, W.D., 2015. CFD simulation of outdoor ventilation of generic urban configurations with different urban densities and equal and unequal street widths. Building and Environment 92, 152–166.

Ribes, A., Caremoli, C., 2007. Salomé platform component model for numerical simulation. Proceedings - International Computer Software and Applications Conference 2, 553 – 564.

Rodriguez, S., 2019. Applied Computational Fluid Dynamics and Turbulence Modeling. Springer Nature Switzerland.

Sagaut, P., 2006. Large Eddy Simulation for Incompressible Flows. Springer-Verlag Berlin Heidelberg.

Salim, S.M., Cheah, S.C., Chan, A., 2011. Numerical simulation of dispersion in urban street canyons with avenue-like tree plantings: Comparison between RANS and LES. Building and Environment 46, 1735–1746.

Selmi, W., Weber, C., Rivière, E., Blond, N., Mehdi, L., Nowak, D., 2016. Air pollution removal by trees in public green spaces in strasbourg city, france. Urban Forestry & Urban Greening 17, 192–201.

Shen, J., Gao, Z., Ding, W., Yu, Y., 2017. An investigation on the effect of street morphology to ambient air quality using six real-world cases. Atmospheric Environment 164, 85–101.

Solazzo, E., Cai, X., Vardoulakis, S., 2008. Modelling wind flow and vehicle-induced turbulence in urban streets. Atmospheric Environment 42, 4918–4931.

Stafoggia, M., Oftedal, B., Chen, J., Rodopoulou, S., Renzi, M., Atkinson, R., Bauwelinck, M., Klompmaker, J., Mehta, A., Vienneau, D., Andersen, Z., Bellander, T., Brandt, J., Cesaroni, G., de Hoogh, K., Fecht, D., Gulliver, J., Hertel, O., Hoffmann, B., Hvidtfeldt, U., Joeckel, K.H., Jorgensen, J., Katsouyanni, K., Ketzel, M., Kristoffersen, D., Lager, A.,

Leander, K., Liu, S., Ljungman, P., Nagel, G., Pershagen, G., Peters, A., Raaschou-Nielsen, O., Rizzuto, D., Schramm, S., Schwarze, P., Severi, G., Sigsgaard, T., Strak, M., van der Schouw, Y., Verschuren, M., Weinmayr, G., Wolf, K., Zitt, E., Samoli, E., Forastiere, F., Brunekreef, B., Hoek, G., Janssen, N., 2022. Long-term exposure to low ambient air pollution concentrations and mortality among 28 million people: results from seven large european cohorts within the elapse project. Lancet Planetary Health 6, E9–E18.

Streichenberger, B., Chakir, R., Jouy, B., Waeytens, J., 2021. Simulation and validation of cfd turbulent airflow at pedestrian level using 3d ultrasonic anemometer in the controlled urban area "sense-city". Journal of Wind Engineering and Industrial Aerodynamics 219, 104801.

Tee, C., Ng, E., Xu, G., 2020. Analysis of transport methodologies for pollutant dispersion modelling in urban environments. Journal of Environmental Chemical Engineering 8, 103937.

Tilloy, A., Mallet, V., Poulet, D., Pesin, C., Brocheton, F., 2013. Blue-based no 2 data assimilation at urban scale. Journal of Geophysical Research: Atmospheres 118, 2031–2040.

Tominaga, Y., Stathopoulos, T., 2007. Turbulent schmidt numbers for cfd analysis with various types of flowfield. Atmospheric Environment 41, 8091–8099.

Tominaga, Y., Stathopoulos, T., 2011. Cfd modeling of pollution dispersion in a street canyon: Comparison between les and rans. Journal of Wind Engineering and Industrial Aerodynamics 99, 340–348.

Tominaga, Y., Stathopoulos, T., 2013. Cfd simulation of near-field pollutant dispersion in the urban environment: A review of current modeling techniques. Atmospheric Environment 79, 716–730.

Tominaga, Y., Stathopoulos, T., 2016. Ten questions concerning modeling of near-field pollutant dispersion in the built environment. Building and Environment 105, 390–402.

Tominaga, Y., Stathopoulos, T., 2018. Cfd simulations of near-field pollutant dispersion with different plume buoyancies. Building and Environment 131, 128–139.

U.S. Environmental Protection Agency, 1999. Nitrogen oxides (nox), why and how they are controlled. Clean Air Technology Center, Information Transfer and Program Integration Division, Office of Air Quality Planning and Standards, U.S. Environmental Protection Agency.

Vos, P., Maiheu, B., Vankerkom, J., Janssen, S., 2013. Improving local air quality in cities: To tree or not to tree? Environmental Pollution 183, 113–122.

Waeytens, J., Sadr, S., 2018. Computer-aided placement of air quality sensors using adjoint framework and sensor features to localize indoor source emission. Building and Environment 144, 184–193.

Wang, X., McNamara, K., 2006. Evaluation of cfd simulation using rans turbulence models for building effects on pollutant dispersion. Environmental Fluid Mechanics 6, 181–202.

World Health Organization, 2016. Ambient air pollution: A global assessment of exposure and burden of disease.

Wu, A., Ren, W., 2020. TiO2 Nanoparticles: Applications in Nanobiotechnology and Nanomedicine. John Wiley & Sons.

Xing, Y., Brimblecombe, P., 2019. Role of vegetation in deposition and dispersion of air pollution in urban parks. Atmospheric Environment 201, 73–83.

Yang, J., Shi, B., Shi, Y., Marvin, S., Zheng, Y., Xia, G., 2020. Air pollution dispersal in high density urban areas: Research on the triadic relation of wind, air pollution, and urban form. Sustainable Cities and Society 54, 101941.

Yassin, M.F., 2011. Impact of height and shape of building roof on air quality in urban street canyons. Atmospheric Environment 45, 5220–5229.

Yusuf, A., Oladipo, H., Yildiz Ozer, L., Garlisi, C., Loddo, V., Abu-Zahra, M., Palmisano, G., 2020. Modelling of a recirculating photocatalytic microreactor implementing mesoporous n-tio2 modified with graphene. Chemical Engineering Science 391, 123574.

Yusuf, A., Palmisano, G., 2021. Three-dimensional cfd modelling of a photocatalytic parallel-channel microreactor. Chemical Engineering Science 229, 116051.

Zhao, Y., Jiang, C., Song, X., 2021. Numerical evaluation of turbulence induced by wind and traffic, and its impact on pollutant dispersion in street canyons. Sustainable Cities and Society 74, 103142.

Zheng, X., Yang, J., 2021. Cfd simulations of wind flow and pollutant dispersion in a street canyon with traffic flow: Comparison between rans and les. Sustainable Cities and Society 75, 103307.